ORIGINAL PAPER

Impact of DWR radial wind on simulation of western disturbances using NCUM-R modeling system

Devajyoti Dutta[1] · A. Routray[1] · Abhishek Lodh[1] · John P. George[1] · A. K. Mitra[1]

Abstract

The present study evaluates the impact of use of radar observations in data assimilation system by simulating the evolution, propagation and intensity of three western disturbances (WDs). Two numerical experiments were conducted viz. CTL and RAD (assimilation of radar radial velocity plus other observations utilized in the CTL) in this study. The initial conditions generated, after assimilation of radial velocity observations in RAD experiment can simulate evolution, characteristics, structure and associated precipitation with WDs properly compared to CTL. The south-westerly wind bias is seen in CTL analyses over the western Himalayan region due to the scarcity of surface and upper air observations in all cases. But the feature clearly improved in the RAD. The northward transport of moisture fluxes from Arabian Sea and spatial distribution of moisture convergence zone around the WDs are well manifested in RAD analyses which closely matched with ERA5 reanalyses in all cases. But strong magnitude of moisture fluxes is noticed in CTL analyses on many occasions. The magnitude, time and spatial pattern of the high vorticity at the mid-troposphere are adequately simulated by the RAD and are well matched with the corresponding ERA5 reanalyses in all cases. The magnitude, evolution and propagation of various kinetic energy budget terms and precipitation are relatively well simulated in the RAD than the CTL in comparison with ERA5 in all cases. Overall, the assimilation of radial velocity into the high-resolution assimilation-forecast system beneficially impacted the rainfall forecasts, which is validated with various statistical skill scores.

1 Introduction

The winter precipitation during December to February months has great important for agriculture activity, power generation and socio-economic needs across the Northern States of India (NSI). Winter rain in North India is mainly associated with the passage of low-pressure system, known as western disturbance (WD). The WDs are upper level synoptic scale weather systems that embedded with the subtropical westerly jet stream (STWJ). The intensity and evolution of the WDs are mainly influenced by the position of STWJ (Hunt et al. 2018a). The frontal nature of the WD is controlled by the thermodynamical interactions between middle latitude and tropical latitudes large-scale flow. The WDs are

migratory systems formed over the Mediterranean Sea and occasionally far west of the Atlantic Ocean that travel eastwards cross over many countries like Iraq, Iran, Afghanistan and Pakistan before entering north India. The position and intensity of WDs are also determined through the associated mechanisms of the moist-air incursions and interactions with the steep as well as intricate orography of the Himalayan ranges. Typically, seven to eight WDs passed over NSI during winter seasons (Pant and Rupa Kumar 1997). The amount of precipitation received due to WDs depends on the intensity and frequency of the WDs passes over NSI. The intense WDs produced heavy rainfall, chill wind conditions and snowfall over the NSI regions during the eastwards passage of the systems (Lang and Barros 2004; Dimri and Mohanty 2009; Hunt et al. 2018b). Hence, it is vital to predict WDs' intensity and eastward progress as they usually create extreme weather conditions over these regions.

In recent decades, the forecast skill of the numerical weather prediction (NWP) models, mainly high-resolution regional models, for prediction of extreme weather events over the Indian region has been significantly improved with the advancement of the representation of physical processes

✉ A. Routray
ashishroutray.iitd@gmail.com; ashishroutray@ncmrwf.gov.in

[1] National Centre for Medium Range Weather Forecasting (NCMRWF), Ministry of Earth Sciences (MoES), A-50, Sector-62, Noida, UP 201309, India

in the model and model dynamics, increase in model resolution, data assimilation techniques, increase of good quality observations, etc. (Vaidya et al. 2004; Mohanty et al. 2011; Osuri et al. 2012; Routray et al. 2016, 2020; Dutta et al. 2018; etc.). In recent years, the simulation or prediction of WDs and associated weather fields using regional models is getting substantial attention among the researchers/operational communities over India even though it is a challenging task due to the steep orography, valley effects, paucity of observations, etc. (Azadi et al. 2001; Hatwar et al. 2005; Dimri and Mohanty 2009; Dimri and Chevuturi 2014; etc.). The study by Dimri et al. (2004) investigated the impact of topography and model resolution using a non-hydrostatic mesoscale model (MM5) to simulate an intense WD event and associated precipitation activities over northwest India and found that the WD evolution, in terms of its 500 hPa level position, intensity and related weather fields are well simulated, when the realistic topography provided to the model. Specific studies by Azadi et al. (2001), Dimri et al. (2004), Dimri and Mohanty (2009), Dimri and Niyogi (2013), Thomas et al. (2014) and Patil and Kumar (2016) extensively examined the role of model physics, spatial horizontal model resolution, topography, and domain size sensitivity to the model simulation of weather features associated with WDs over north India. Thomas et al. (2018) evaluated the importance of proper representation of the land-use and land-cover data in the weather research and forecasting (WRF) model on the simulation of precipitation over NSI during the passage of WDs. However, the above cited studies have yielded mixed results. Further improving the forecast skill of regional models by providing accurate initial conditions to the model is an important aspect. Particularly for WDs, a major problem is the unavailability of surface and upper air observations to utilize it in the assimilation system (Hatwar et al. 2005). Furthermore, the DWR extends its capacity with dual polarization, giving microphysical characteristics of precipitation associated with extreme weather events (Dutta et al. 2016). The remotely sensed observational data can play a major role to enhance the model initial conditions through its assimilation. Rakesh et al. (2009) suggest that the assimilation of moisture and temperature profiles from satellite through 3DVAR assimilation considerably improved the precipitation intensity and other meteorological variables associated with the WDs.

The Indian Meteorological Department (IMD) has recently expanded its Doppler Weather Radar (DWR) network over north India. The DWR provides high-resolution spatio-temporal information of radial wind and reflectivity (precipitation) associated with different weather conditions (Dutta et al. 2011, 2017). Furthermore, the DWR extends its capability with dual polarization, which gives microphysical characteristics of precipitation associated with extreme weather events (Dutta et al. 2016). Thus, the knowledge on

the characteristics of the precipitable system and its movement enhanced the now-casting and short-range forecasting capabilities. Many previous studies suggested that the utilization of DWR observations into a data assimilation system improves the representation of the meso-convective systems in the model initial conditions. This can help to improve the forecast skill substantially with regard to the evolution of the convective systems and even intensity and location of associated rainfall (Gao et al. 1999; Xiao et al. 2007; Abhilash et al. 2007; Routray et al. 2010, 2013; Prasad et al. 2014; Osuri et al. 2015; Dutta et al. 2019; etc.). However, no such study evaluated the impact of the assimilation of the Indian DWR radial velocity data on the simulation of the WDs.

The prime objective of the present study is to assess the importance of Indian radar observations in correcting the WD environment and in turn improving the forecasts of precipitation and other meteorological fields associated with it. For this purpose, we considered three WDs experienced during 21–23rd January 2019; 7–10th February 2019 and 27–29th January 2020, which affected the NSI region during their eastward passage. The paper is divided into the following sections, the synoptic situation associated with the WDs is presented in Sect. 2. Section 3 provides a brief description of the forecast model and the data assimilation systems, while numerical experiments carried out in this study are summarized in Sect. 4. The methodology applied to evaluate the study results obtained from the numerical experiments is provided in Sect. 5. Section 6 details the results and discussion obtained from the current study and Sect. 6 presents the summary and conclusions of the study.

2 Synoptic conditions associated with WDs

2.1 Case1 (21–23rd January 2019)

An intense WD along with an induced low-pressure system affected the western Himalayan region on 21st January 2019 and the plains of northwest India. Under its influence, heavy snowfall occurred over Jammu and Kashmir (J&K) and adjoining areas on 21st January 2019. The WD was further intensified by the incursion of moisture from the Arabian Sea as it moved eastward. During 22nd and 23rd January 2019, the WD caused widespread heavy precipitation over Punjab, Haryana, west Utter Pradesh and isolated to scattered rainfall over north Rajasthan and east Utter Pradesh. Hailstorm/thundershower activity was also observed few places over central-eastern parts of India due to interaction between easterlies and westerlies. Dense to very dense fog was experienced along with cold wave conditions over Punjab, West Rajasthan, Haryana, Chandigarh and Delhi regions during the period. The satellite imagery (Fig. 1a) shows strong convective cloud band over Northern States
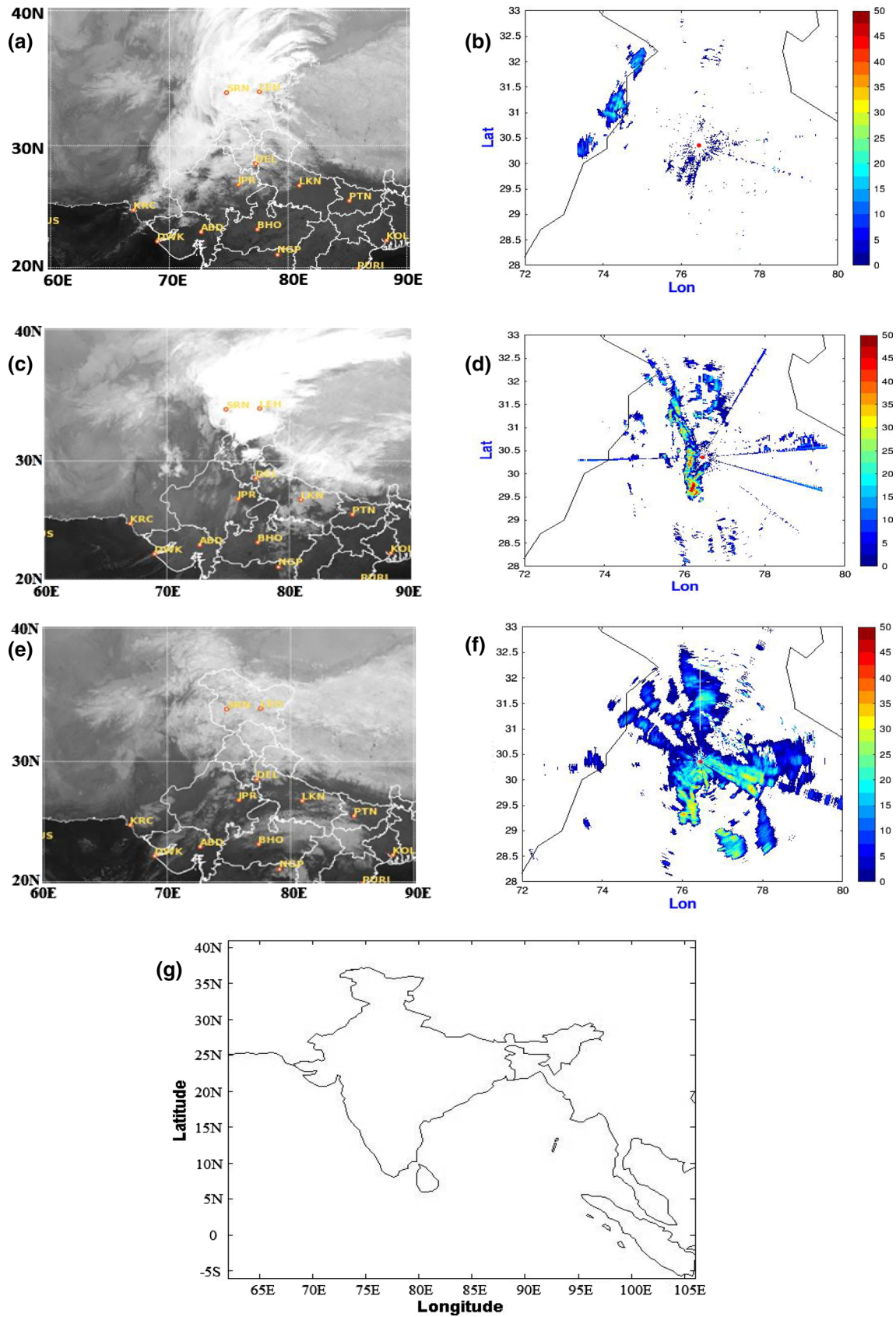
Fig. 1 **a** Satellite imagery and **b** Reflectivity (dBz) from Patiala DWR for Case 1 valid at 00 UTC 21 January 2019. **c–d** and **e–f** are same as (**a**, **b**) but for Case 2 and Case 3 valid at 00 UTC 7th February 2019 and 28 January 2020, respectively. **g** Model domain

of India and adjoining areas. The high reflectivity (Fig. 1b) from Patiala DWR is also noticed over Pakistan and northwest parts of India.

2.2 Case 2 (7–10th February 2019)

A WD persisted on 7th February 2019 over north Pakistan and the adjoining area extending up to 7.6 km above mean sea level with a trough at 3.1 km. This induced cyclonic circulation ran southwestwards to the north Arabian Sea and further, it ran up to the east central Arabian Sea to the north of latitude 15° N on 8th February 2019. The WD was gradually intensified due to the pumping of high moisture from the Arabian Sea, strong wind confluence at lower levels and divergence at the upper troposphere during 8th and 9th February 2019. Under its influence, heavy to very heavy rainfall/snowfall at isolated places over the western Himalayan region. The widespread rain/thundershowers along with hailstorm activities also observed over J&K, Ladakh, Himachal Pradesh, Uttarakhand, Punjab, Haryana, Rajasthan, West UP and Delhi NCR regions during the period. During its eastward movement, the fairly widespread to widespread rainfall occurred over other parts of the country. Many stations observed 3–14 cm rainfall over the Northern States of India during the period as reported by IMD. After the passage of WD, the north parts of India observed dense to very dense fog during the period. The INSAT-3D image shows strong convective cloud cover over north India (Fig. 1c). It is also seen that strong reflectivity of more than 45 dBZ has been observed by the Patiala DWR station (Fig. 1d) during 7th February 2019. Both the satellite and DWR images suggested that the intense WD persisted over the NSI regions.

2.3 Case 3 (27–29th January 2020)

A WD as a cyclonic circulation at 3.1 km above mean seal level was observed over Afghanistan and the neighborhood on 27 January 2020. Under its influence, an induced low-pressure system extended up to 1.5 km above mean sea level was developed over west Rajasthan and adjoining areas in lower tropospheric levels on this day. The WD moved eastward and caused light to heavy precipitation over the western Himalayan region from 27th January. The WD became more intensified due to the incursion of fresh moisture from the Arabian Sea at lower and upper tropospheric levels, increasing the divergence at upper tropospheric levels. The intensity and spread of WD was increased and it reached the peak stage on 28th January 2020. Therefore, light to moderate rainfall occurred over J&K, Himachal Pradesh, Uttarakhand, Punjab, Haryana, Delhi and NCR, Uttar Pradesh, North Rajasthan on 28th and 29th January. As per IMD report, many stations over the region received 2–6 cm rainfall within 24 h during the period. As the system moved

eastward, the other parts of the country also received isolated or scattered rainfall/thundershower during the period. After the passage of the WD, the dense fog was also experienced over many places over NSI region due to favorable atmospheric conditions. The INSAT-3D imagery shows convective clouds over NSI regions (Fig. 1e). The Patiala (30.35° N/76.44° E) DWR station (Fig. 1f) is showing high amount of reflectivity (~35 dBz) surrounding the region during 28th January 2020.

3 Forecast modeling and data assimilation systems

The regional version of the National Centre for Medium Range Weather and Forecasting (NCMRWF) Unified Model (NCUM-R) is operationally running at NCMRWF with horizontal grid spacing ~4 km (1200×1200 pts in the domain) and 80 vertical hybrid-height levels extending up to ~38.5 km. The non-hydrostatic, terrain-following hybrid-height vertical coordinate NCUM-R model is configured over the Indian domain (62°–106° E, 6°–42° N; Fig. 1g), which generates three days numerical weather forecasts daily twice at 00 and 12 UTC. The model is embedded with various types of physical parameterization schemes and also with advance dynamic core (Cullen et al. 1997; Wilson and Ballard 1999; Lock et al. 2000; Davies et al. 2005; Clark et al. 2011; etc.). The high-resolution NCUM-R forecasting system has fully explicit treatment of convection. The primary model variables are Exner pressure, horizontal (u), meridional (v) and vertical (w) components of wind, potential temperature, density and three components of moisture (cloud ice, cloud water and water vapor). The incremental-based four-dimensional variational (4DVAR) data assimilation (DA) algorithm (Rawlins et al. 2007; Ballard et al. 2016) has been adapted to produce high-resolution analysis, which is used as initial conditions for the NCUM-R forecast. Details of the high-resolution NCUM-R modeling system and 4DVAR data assimilation scheme can be found in Routray et al. (2020) and Dutta et al. (2019).

4 Numerical experiments

The high-resolution (4 km) NCUM-R model (UM version 10.8) along with 4DVAR DA system is used to full fill the prime objective of the present study by simulating two WDs. Figure 1g depicts the experimental domain considered for this study. Two numerical experiments are conducted viz. first experiment named as CTL (assimilated various conventional and non-conventional observations accessible at NCMRWF, https://www.ncmrwf.gov.in/t574-model/obs_monitor/Daily_MR_hh.pdf. where 'hh' represents the

synoptic hours) and second experiment i.e. RAD (assimilated DWR radial velocity along with all observations utilized in CTL experiment). The 4DVAR DA technique is used in both experiments to produce high-resolution analysis, used as the initial condition for NCUM-R forecast. The global NCUM model (12 km) forecast fields are used as lateral boundary conditions for the NCUM-R model, updated every three hours. In the present study, the DWR reflectivity data are not assimilated because of erroneous in the reflectivity observations (clutters, beam broadening, Anomalous Propagation, refraction, etc.) due to the steep and complex orography of the Himalayan ranges. The details of the NCUM-R model configuration and physical parameterization schemes used are presented in Table 1. The model integration starts from the initial times 00 UTC of 21st January 2019, 7th February 2019 and 28th January 2020 and up to 72 h forecast are produced for Case 1, Case 2 and Case 3, respectively. Figure 2a–c shows the amount of observations obtained from various platforms through Global Telecommunication System (GTS) as well as cumulative radial velocity observations from various DWR stations, which are assimilated in the 4DVAR system for Case 1 to Case 3 to produce analysis valid for 00 UTC of 21st January 2019, 7th February 2019 and 28th January 2020, respectively. The radial velocity observations from individual DWR stations over the experimental domain are depicted in Fig. 2d–f for Case 1–Case 3, respectively. It is noticed that the good number of DWR radial wind observations from DWR stations located over north India are assimilated in all the cases.

The quality control (QC) of DWR observations is an essential before assimilating them into a high-resolution regional model. We have applied various basic QC checks, which are described in Kasimahanthi et al. (2017). In the next step also, various QC checks, mainly compared against the background (short forecast), are performed within the observation processing system (OPS) before the assimilation. We have not considered observation with large innovation, observation minus background (O–B), beyond 10 m/s, because it may increase the gross error and slower the convergence during the assimilation process (Stewart et al. 2008). When the DWR observations very close, far away from the radar as well as outside of time ranges are also discarded. The detailed procedure for pre-processing, QC checks, super-obbing processes of DWR observations as well as the details of the observation operator can be found in Dutta et al. (2019).

5 Methodology

The model simulated rainfall obtained from both the numerical experiments are evaluated using various statistical verification metrics such as Structure-Amplitude-Location (SAL), Fractions Skill Score (FSS) and Equitable threat score (ETS). These statistical skill scores are calculated against "NCMRWF-IMD rainfall analysis (0.25° resolution)," which is a merged analysis product of global precipitation measurement (GPM) satellite rain estimate and rain gauge measurement data (Mitra et al. 2009).

The Structure-Amplitude-Location (SAL; Wernli et al. 2008, 2009) is a spatial verification method that evaluates the rainfall fields over a fix gridded verification domain through identifying and comparing the objects from the model forecast and observed fields at a particular time and

Table 1 Brief descriptions of model configuration and physical parameterization schemes used in the study (Routray et al. 2021)

| Parameters	NCUM-R model configuration
Governing equations	Non-hydrostatic compressible equations and a terrain-following hybrid-height vertical coordinate (model top upto ~ 38.5 km)
Horiz. resolution (N–S×E–W)	~ 4.4 km (0.04*0.04) with grid points: 1200×1200
Vertical layers	80 terrain following hybrid-height
Model time step	60 s
Analysis system	4DVAR provides initial conditions to NCUM-R forecast model
Boundary condition	From global NCUM that interpolated to regional domain and updated 03 hrly
Spatial discretization	Finite difference method
Time integration	Semi-implicit, semi-Lagrangian, predictor corrector numerical scheme
Radiation process	Spectral band radiation
Surface process	Joint UK Land Environment Simulator (JULES) land surface Scheme
PBL process	First order non-local boundary layer scheme
Convection process	Explicit convection
Microphysics	Improved mixed-phase scheme
Gravity wave drag	A new orographic drag scheme which contains better physical basis
Surface boundary condition	Surface Analysis + Climatology
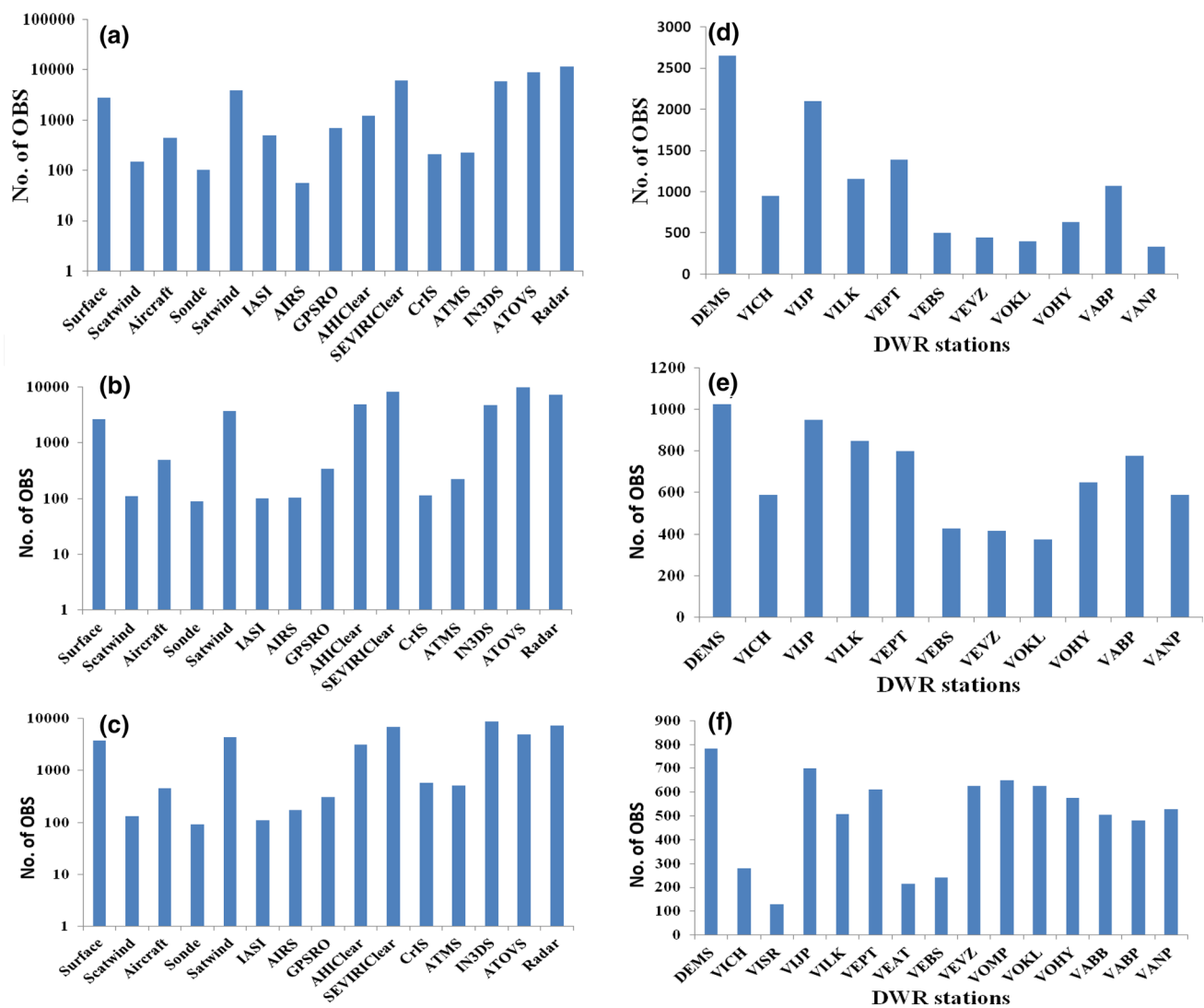
Fig. 2 Number of observations from various platforms used in the assimilation cycle **a** Case 1, **b** Case 2 and **c** Case 3 valid at 00 UTC 21st January 2019, 7th February 2019 and 28th January 2020, respectively. **d**–**f** are same as (**a**–**c**) but radial velocity from individual DWR stations

provides error for three components. The "S" (Structural component) matches the volume of simulated precipitation objects with observed fields and in order to provide their size and shape. The range of "S" value varies between − 2 and + 2. The positive (negative) value of the "S" suggests the model predicted precipitation objects widespread or too flat (too sharp or small) as compared to the observed precipitation fields. The amplitude component (A) calculates the domain averaged rainfall difference between the model forecasts and observations. The value of "A" varies between the ranges − 2 to + 2. The positive (negative) value of "A" signifies overestimation (underestimation) of total rainfall. The values of "A" close to − 2 indicate the precipitation events almost missed in the model forecast. In contrast, the values of "A" close to 2 indicate the false alarms in the model forecast. Finally, the location component (L) combines two

parts, one part is the distance between the mass centers of the model forecasted and observed rainfall fields over the domain and the 2nd part measures the weighted average displacement of the individual rainfall objects from the mass centers of total precipitations field. The value of "L" varies between 0 and 2. Here, the zero value of "L" can be obtained for a model forecast when the center of mass as well as the mean displacement between individual rainfall objects and the center of mass of total fields fully agreed with the observations. The perfect forecast can be obtained when all the three components of SAL having zero value. The details of the mathematical expression and physical significance of individual terms of SAL can be found in the studies of Wernli et al. (2008, 2009) and Lawson and Gallus Jr (2016); etc.

The Fractions Skill Score (FSS) is a neighborhood-based verification method used to verify the precipitation

forecast against observations (Roberts and Lean 2008; Ebert 2008, 2009). The FSS primarily depends on the scale of the user specified area and also rainfall threshold. This approach is different from the other object-based methods, where the exact match between the rainfall objects is obtained from forecast and observation. Conceptually, the FSS method directly compares the fractional coverage of rainfall events in the given areas surrounding the forecasts and observations, regardless of the exact location of rainfall objects within the prescribed window (area). The FSS is calculated as a ratio of the fractions Brier Score and the sum of the mean squared observation as well as forecast fractions. The mathematical expression of FSS is given as below:

$$
\text{FSS} = 1 - \frac{\frac{1}{N} \sum_{i=1}^{N} \left(P_{\text{fcst}} - P_{\text{obs}} \right)^2}{\frac{1}{N} \left(\sum_{i=1}^{N} P_{\text{fcst}}^2 + \sum_{i=1}^{N} P_{\text{obs}}^2 \right)},
\tag{1}
$$

where N is the number of grid points within the verification domain, P_{fcst} and P_{obs} is the fractional coverage of forecast and observation, respectively. The FSS varies between 0, means a complete mismatch, to 1, for a perfect match.

Initially, the reflectivity data converted into Cartesian coordinates at 1-km height above the ground level before calculating rainrate (mm/h) using Marchall-Palmer global Z–R equation ($Z = 200R^{1.6}$, Marshall and Palmer 1948). The rainrate data are then applied an advection correction scheme to minimize the temporal sampling effect. These data are then aggregated into hourly rainrate maps (Anagnostou and Krajewski 1999). The model simulated rainrate is compared with the DWR-derived rainrate.

The equitable threat score (ETS) or Gilbert skill score varies between 0 and 1. The ETS value equal to 1 indicates a perfect forecast and 0 indicates no skill for the forecast. One can say, the model overestimated or underestimated the rainfall when the ETS value higher or lower than 1, respectively. The details about the ETS can be found in Routray et al. (2021).

The kinetic energy (KE) budget terms over the domain (24°–38° N; 68°–82° E) has been computed for the WDs. The KE is produced by conversion of the available atmospheric potential energy and it is also dissipated by friction. The generation of the KE due to the conversion of the available potential energy is usually described through a process where the warmer in ascending motion and colder air in descending motion. The KE is exclusively determined through the horizontal flow of the atmosphere. The KE budget equation in Eulerian frame of reference (Kung and Baker 1975; Raju et al. 2011) can be written as

$$
\frac{\partial K}{dt} + \vec{\nabla} \cdot K\vec{V} + \frac{\partial (K\omega)}{\partial p} = -\vec{V} \cdot \vec{\nabla}\varphi + D,
\tag{2}
$$
$\quad(a)\qquad(b)\qquad\quad(c)\qquad\quad(d)\qquad(e)$

where K is kinetic energy per unit mass, $\vec{V}(u, v)$ is two-dimensional horizontal wind vector, p is the pressure, ω is the vertical velocity in p-coordinate, φ is the geopotential, D is the dissipation frictional force, t is the time and $\vec{\nabla}$ is the horizontal gradient operator. The first term (Eq. 2a) denotes the local rate of change of KE. The second term (2b) describes the horizontal flux divergence or horizontal transport of the KE out of the domain and the third term (2c) indicates the vertical flux divergence of the KE. The term-2d on the right-hand side represents KE generation through cross-isobaric flow. The process may be adiabatic or thermodynamically reversible for the generation/destruction of the KE. The positive value of the term-2d implies the production of KE through conversion of available potential energy, while the –ve value means the destruction of KE that backs to the available potential energy of the atmosphere. Thus, it measures the cross-isobaric or ageostrophic acceleration of the flow (if geostrophic flow, the term became zero). The last term (2e) denotes the dissipation of KE through turbulent frictional processes i.e., generally calculated as a residue.

In this current study, we analyzed few terms of KE budget equation. The term 2a, is calculated as the time change in the kinetic energy level during 1-h time period centered at the observation and forecast period for which the energy balance is computed. The gridpoint values of terms 2b and 2d are calculated as the line integral with the horizontal wind components at grid points on the defined boundary.

6 Results and discussion

6.1 Impact on model analyses

It is necessary to understand how the model initial conditions (analyses) differ after the assimilation of DWR radial velocity from the CTL analyses before assessing its impact on the model simulations. Therefore, this section describes the changes in the model analyses after assimilation of DWR radial velocity (RAD) with respect to the CTL analyses through a comparative study.

To evaluate the efficacy of assimilation system, a comparison is made between the mean of background innovation (observation minus first guess i.e. O–B) and the mean of analysis innovations (observation minus analysis i.e. O–A). The root mean square errors (RMSEs) of O–A from CTL and RAD experiments of all the WD cases are shown in Table 2. From Table 2, it can be noticed that the RMSE of O–A of various meteorological variables from RAD experiment is relatively less than the RMSE of O–A from CTL.

Table 2 Mean RMSE of O-A for all the WD cases

WD cases (at model initial time)	Different model variables									
	u-wind (m/s)		v-wind (m/s)		T (°K)		Q (g/kg)		Radial wind (m/s) (O–B)	
	CTL	RAD	CTL	RAD	CTL	RAD	CTL	RAD	CTL	RAD
Case 1 (00 UTC 21st Jan. 2019)	2.37	2.28	2.35	2.13	1.44	1.25	2.19	2.05	–	1.92 (3.12)
Case 2 (00 UTC 07th Feb. 2019)	3.29	3.14	3.46	3.08	1.42	1.30	1.89	1.65	–	1.83 (2.05)
Case 3 (28th Jan. 2020)	2.97	2.78	2.76	2.42	1.56	1.35	2.35	2.12	–	2.96 (3.6)

Similarly, the RMSE of O–A for radial velocity is reduced with respect to the RMSE of O–B. This clearly suggests that the assimilation of the DWR radial wind has a positive (beneficial) impact on the analysis.

The wind and geopotential height at 500 hPa from ERA5 reanalyses and the systematic bias between the model analyses from CTL and RAD experiments and ERA5 reanalyses are presented in Fig. 3a–c; d–f and g–i for Case 1–Case 3, respectively. ERA5 reanalysis (Fig. 3a) shown a cyclonic circulation lay along the longitude around 67° E mainly over the Afghanistan region and the band of strong magnitude winds about 20–30 m/s noticed along the south and southeastern sector of the system. Both the model analyses (Fig. 3b and c) are shown eastward shift of cyclonic circulation. The CTL analysis (Fig. 3b) shows more intense wind flow along the cyclonic circulation corresponding to the ERA5 reanalysis. This indicates more intense cyclonic circulation in the CTL analysis as compared to the ERA5 reanalysis. However, the positive bias of the wind magnitude seen in the cyclonic circulation of CTL analysis is considerably reduced in the RAD analysis (Fig. 3c) after the assimilation of radar radial velocity observations. It is also noticed that intense positive bias of wind has been produced by the CTL analysis over the western Himalayan region due to the presence of stronger storm in the analysis. The proper representation of cyclonic circulation in the RAD analysis (Fig. 3c) after assimilation of radial wind is reduced magnitude of wind speed bias substantially over the western Himalayan region. The RAD analysis also underestimated the wind magnitude over certain pocket of the northwest region compared to the ERA5 reanalysis (Fig. 3a). The geopotential height in the CTL analysis is stronger than the ERA5 reanalysis. But, the geopotential height in RAD analysis and ERA5 are shown good agreement when the wind speed biases are compared. In Case 2, the ERA5 (Fig. 3d) is depicting more intense WD over the Indo-Pakistan region associated with the strong wind of 25–40 m/s in the area of the cyclonic circulation. The WD gradually intensified and formed a midtropospheric trough during the eastward movement over the region. The CTL analysis (Fig. 3e) shows a strong positive wind speed bias over the western Himalayan region like in Case 1. At the same time, the positive bias over the region is appreciably reduced in the RAD analysis (Fig. 3f) after

the assimilation of radar radial velocity observations. The positive bias of geopotential fields is also seen in the CTL analysis (Fig. 3e), which is missing in the RAD analysis. The spatial extent of the cyclonic circulation associated with the WD is reproduced well in the RAD analysis (with respect to ERA5) compared to the CTL analysis. In Case 3, similar distribution i.e., positive biases over northwest India as well as in some areas of Pakistan and Afghanistan, like in Case-1 and 2, is also noticed in the CTL analysis (Fig. 3h). The CTL analysis shows intense cyclonic circulation associated with the WD compared to the ERA5 reanalysis (Fig. 3g). However, the magnitude and pattern of wind associated with the WD are reasonably well characterized in RAD analysis (Fig. 3i) and very closely agree with the ERA5 reanalysis. CTL analyses generally show south-westerly bias over the western Himalayan region during all the WD cases. It can be inferred that, from all the cases, the large positive bias seen in CTL analysis may be the unavailability of sufficient surface and upper air observations over the Himalayan regions. The DWRs provide good spatial/temporal resolution radial velocity observations over the regions help to reduce the scarcity of wind observations over the Himalayan regions. Hence, the assimilation of radar radial velocity observation positively impacted the analysis, which helps to improve the representation of the wind flow associated with the WD more accurately. Table 3 shows RMSE of u- and v-components of wind analysis calculated with respect to the upper air observations obtained from Patiala, Delhi and Lucknow RS/RW stations for all the WD cases. It is clear that the RMSE of zonal and meridional wind components is less in the RAD analyses for all the cases than the CTL analysis. The spatial distribution of vertically integrated moisture flux (VIMT; kg/m/s) and moisture convergence (kg/m²/s; shaded) from CTL and RAD analyses along with the corresponding ERA5 reanalyses values are depicted in Fig. 4a–c; d–f and g–i for Case 1–3, respectively. In Case 1, the CTL analysis (Fig. 4b) is showing strong moisture convergence over the northwest of India as well as western Himalayan regions (Fig. 4a). However, the moisture convergence is reduced appreciably over the regions in the RAD analysis (Fig. 4c) during the period, which is in corroboration with the ERA5 reanalyses. It is also noticed that strong south-westerly moisture transport in the CTL analysis caused the enhancement
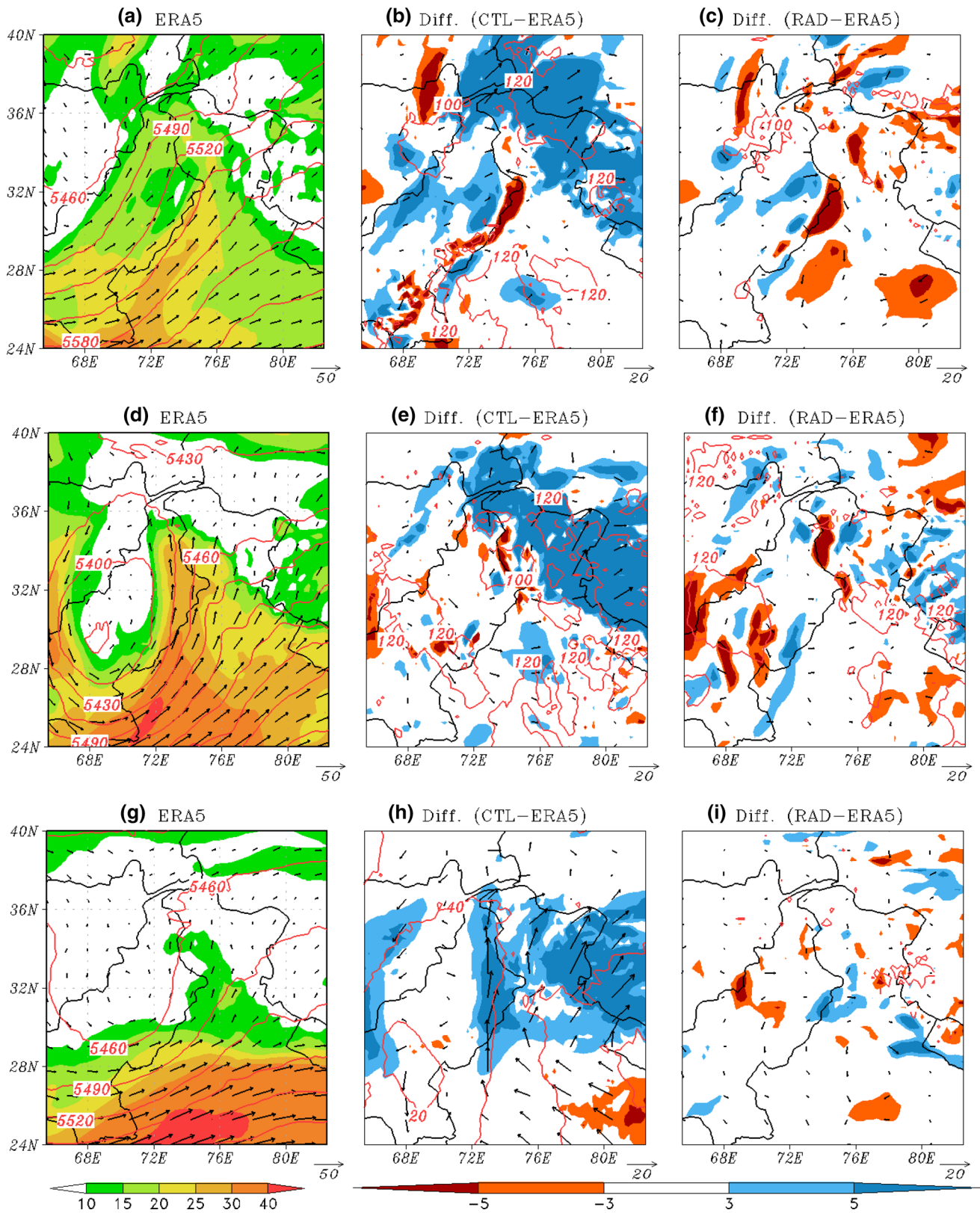
Fig. 3 Wind (m/s, magnitude shaded) and geopotential (m, contour) at 500 hPa for **a** ERA5; **b** difference between CTL-ERA5 and **c** difference between RAD-ERA5 of Case 1 at model initial time valid at 00 UTC 21st January 2019. **d–f** and **g–i** are same as (**a–c**) but for Case 2 and Case 3 valid at 00 UTC 7th February 2019 and 28th January 2020, respectively

Table 3 RMSE of wind from both the experiments calculated based on RS/RW observations from Patiala, Delhi and Lucknow

WD cases (00 UTC of)	Model initial time			
	u-wind (m/s)		*v*-wind (m/s)	
	CTL	RAD	CTL	RAD
Case 1 (21st Jan. 2019)	1.89	1.74	4.53	3.23
Case 2 (07th Feb. 2019)	1.92	1.59	4.13	3.13
Case 3 (28th Jan. 2020)	1.83	1.67	2.15	1.08
Mean	1.88	1.66	3.60	2.48

of the moisture flux over the regions. The feature is well produced in the RAD analysis after the radar radial velocity observations are assimilated, closely matching with the ERA5 reanalyses. It is also observed that the distribution of intense patches of flux along the western border of Rajasthan and Punjab in RAD analysis is well correlated with the location of the observed radar reflectivity observation (Fig. 1b). In Case 2, the ERA5 reanalyses (Fig. 4d) is showing strong moisture convergence over plains of Punjab and Haryana regions which is spatially extended even up to Delhi. The zone of moisture convergence over these plains in the RAD analysis (Fig. 4f) is well matched with the corresponding verification reanalyses (ERA5). However, the CTL analysis (Fig. 4e) is showing intense moisture convergence over the domain. The orientation of moisture transport from the Arabian Sea is well characterized in the RAD analysis compared to the CTL analysis. The feature is reasonably well correlated with corresponding ERA5 reanalyses. The elongated feature of intense moisture flux from RAD analysis (Fig. 4f) over the northern plains matches even well with the radar observed reflectivity (Fig. 1d). The high amount of moisture convergence has built up along the windward side of the western Himalayan region, suggesting the effect of the orography (Dimri 2012). In Case 3, the ERA5 reanalyses (Fig. 4g) is showing cyclonic circulation associated with WD along the northwestern edge of Rajasthan and Punjab during the period. The cyclonic circulation over the region is well characterized in the RAD analysis (Fig. 4i) and is very closely matched with the verification reanalyses. This feature is missing in the CTL analysis (Fig. 4h) during the period. The northward transport of moisture fluxes from the Arabian Sea and spatial distribution of moisture convergence zone around the cyclonic circulation are well pronounced in the RAD analysis, matching well with the ERA5 reanalyses. However, the intense transport of moisture fluxes resulted due to the high moisture convergence zones over the whole domain is noticed in the CTL analysis. These patterns of moisture convergence zones are not seen in the ERA5 reanalyses. The study by Dimri (2007) suggested that a high amount of transport of potential energy and moisture from the Arabian Sea toward the northern Indian plains interacts

with the westerlies flow associated with the WD and gradually enhances the storm's intensity. The orientation of moisture transport and moisture convergence zones over the northwest of India is well represented in RAD in comparison with the previous studies of Dimri (2007, 2012) and Dimri and Chevuturi (2014).

6.2 Impact on model forecast

6.2.1 Wind fields

The day-1 forecast of wind at 500 hPa from CTL and RAD simulations along with verified reanalysis (ERA5) is depicted in Fig. 6a–c; d–f and g–i for Case 1–3, respectively. The subjectively analyzed upper-air wind field at 500 hPa from IMD is presented in Fig. 5a and b for Case 1 and Case 2, respectively. In Case 1, the ERA5 (Fig. 6a) shows a well-defined and close cyclonic circulation over the northwest of Afghanistan. The subjectively analyzed wind field of IMD (Fig. 5a) at 500 hPa is clearly showing a well-marked trough over the region extended up to lower latitudes around 25° N. The trough is simulated by the RAD experiment (Fig. 6c) over the region. The position and orientation of the trough are closely resembled with the IMD analyzed wind field (Fig. 5a). However, the CTL simulation (Fig. 6b) shows a close cyclonic circulation over the region like in ERA5 reanalysis, which is anomalous as per IMD analyzed wind field. The magnitude of wind at 500 hPa (Fig. 5a) over Srinagar (34.05° N; 74.5° E) and Delhi (28.41°N; 77.01° E) upper air stations was observed about 15 m/s and 28 m/s during the period. The magnitude of wind at 500 hPa in the RAD (CTL) simulation is about 14 m/s (23 m/s) and 30 m/s (25 m/s) over these stations. The magnitude of wind from RAD simulation is closer to the IMD observations than the CTL simulation. From Fig. 6a, a, strong elongated spatial distribution of wind with magnitude of ≤ 40 m/s is noticed over 24°–28° N and 65°–80° E region. The intensity and spatial distribution of wind over the region are considerably well simulated by the RAD experiment in comparison with ERA5 reanalysis. The magnitude of wind is closely corroborated with the RS/RW observations over the region. On the other hand, the CTL simulation is shown the diminution of wind magnitude over the region during the period while compared to the RAD and ERA5. In Case 2, the subjectively analyzed wind fields from IMD (Fig. 5b) show a strong closed cyclonic circulation associated with the WD over the north Pakistan region during 00 UTC 08th February 2019. The cyclonic circulation associated with the storm as well as the strong magnitude of wind about 25–40 m/s over extreme northwest and southwest sectors of the WD is well captured by the RAD simulation (Fig. 6f) as indicated in the corresponding
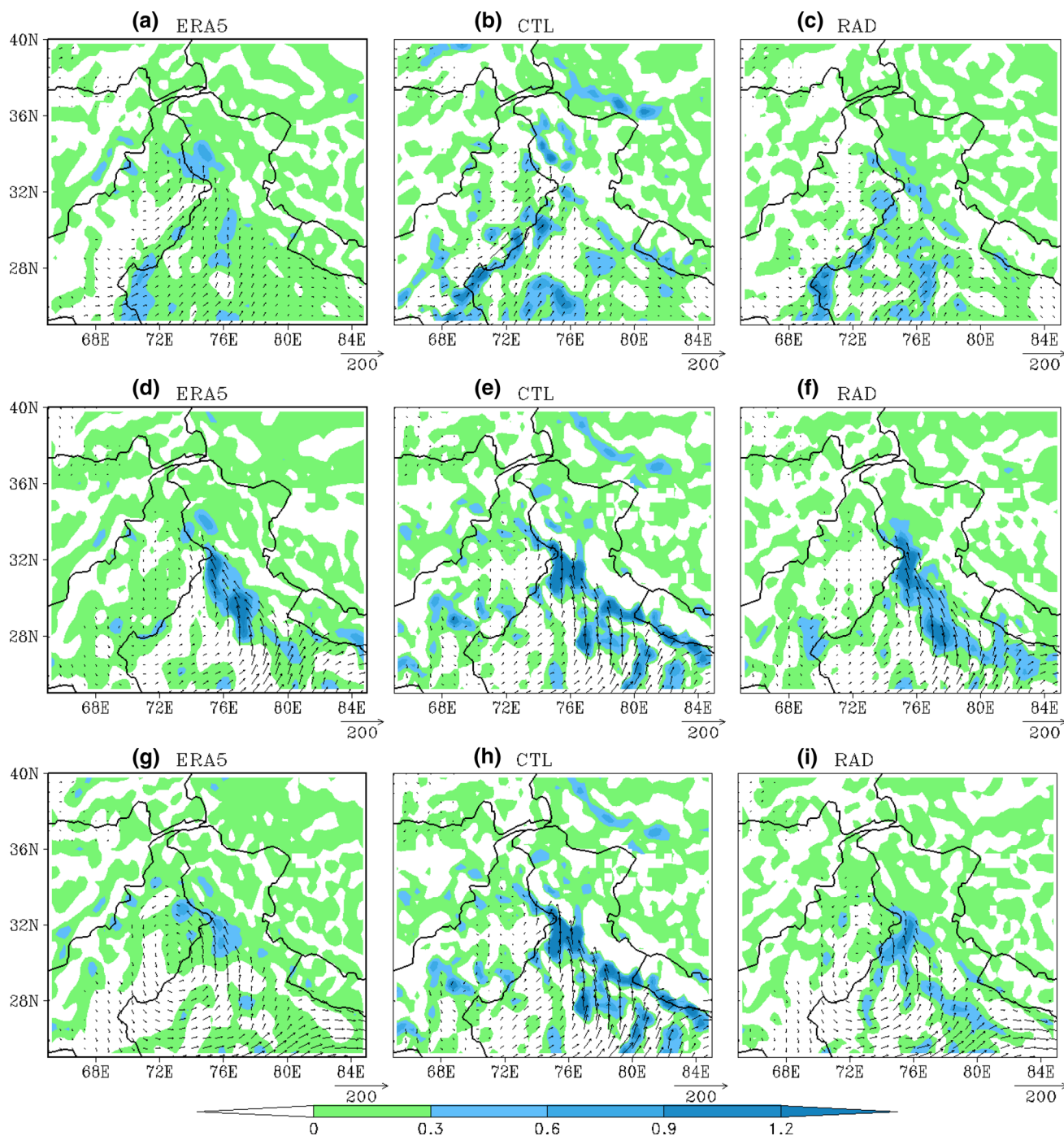
Fig. 4 Vertical integrated moisture flux (VIMT; kg/m/s; vector) and moisture convergence (kg/m^2/s; shaded) integrated up to 400 hPa for **a** ERA5; **b** CTL and **c** RAD analyses of Case 1 at model initial time valid at 00 UTC 21st January 2019. **d–f** and **g–i** are same as (**a–c**) but for Case 2 and Case 3 valid at 00 UTC 7th February 2019 and 28th January 2020, respectively

verification analysis (ERA5; Fig. 6d). The position of the cyclonic circulation is closely matched with the IMD analyzed wind fields (Fig. 5b). The CTL experiment (Fig. 6e) can neither simulate the closed cyclonic circulation over the region nor show the wind magnitude at various sectors of WD affected regions similar to ERA5 and RAD. The

observed wind over Srinagar and Patiala (30.2° N; 76.28° E) upper air stations from Fig. 5b was about 10 m/s and 17 m/s during the period. The simulated magnitude of wind over the stations (~ 8.5 m/s and ~ 13 m/s) is substantially increased with radar radial velocity observation assimilated analysis compared to the CTL (~ 7 m/s
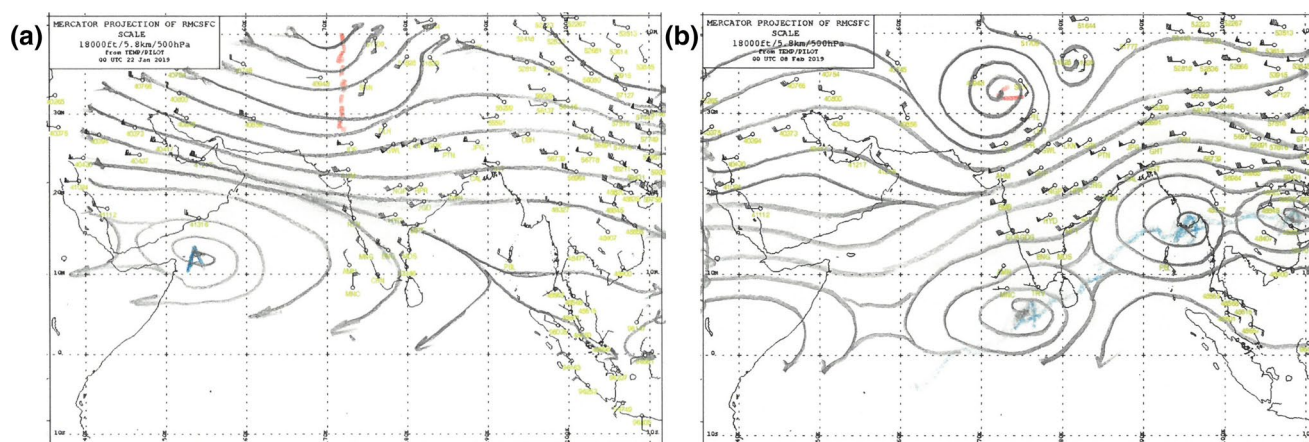
Fig. 5 Upper-air chart of streamline analyses along with observed wind (kts) at 500 hPa for **a** Case 1 and **b** Case 2 valid at 00 UTC 22nd January 2019 and 8th February 2019, respectively (*Courtesy: CRS, IMD, Pune*)

and ~ 9 m/s). Similarly in Case 3, the cyclonic circulation over Afghanistan and Pakistan region is simulated by the RAD experiment (Fig. 6i) is closer to the reanalysis (Fig. 6g). The simulated cyclonic circulation associated with the WD is missing or farther away from its reanalysis location in CTL experiment (Fig. 6h). The magnitude of wind over the latitudinal belt between 24° and 28° N is well simulated in the RAD, which is similar to the ERA5 reanalysis. The model simulated wind fields could not be able to compare with the IMD analyzed wind fields due to the unavailability of upper-air analysis charts. The RMSE for wind speed (m/s) are computed at different pressure levels for both the simulations against the IMD upper-air observations (10 RS/RW stations) available over the specific domain (23°–36° N and 72°–85° E). The model simulated wind speed is interpolated to the observation points through bi-linear interpolation before the calculation of RMSE. The RMSE of day-1 forecast of wind speed at different pressure levels is presented in Table 4. It is clearly noticed that the RMSEs of wind speed at various pressure levels are noticeably reduced in the RAD simulations compared to the CTL simulations in all the cases. Many previous studies inferred that assimilation of DWR radial velocity observation into the high-resolution mesoscale models improved the simulation of convective weather systems (Gao et al. 1999; Xiao et al. 2005; Abhilash et al. 2007; Routray et al. 2013; Prasad et al. 2014; Dutta et al. 2019; etc.). It is noted that the mean RMSE for Case 1–3 is reduced by 25%; 14% and 15% in the RAD compared to CTL simulation (Table 4), respectively. Overall the structure and wind speed associated with the WDs are reasonably well simulated by the RAD compared to the CTL simulation, which are comparable with the verification reanalyses (ERA5) as well as IMD subjectively analyzed wind fields.

6.2.2 Vorticity

The spatial averaged (24°–40° N and 65°–82° E) time-pressure cross-section of vorticity ($\times 10^{-5}$ s^{-1}), from the model simulation (up to 72 h) of CTL and RAD along with the verification reanalyses (ERA5) for Case 1–3 is depicted in Fig. 7a–c; d–f and g–i, respectively. The vertical structure of the vorticity in ERA5 reanalysis (Fig. 7a) shows that the positive vorticity field extended all the way from the surface to the upper atmosphere. As per the IMD report, the WD was intensified due to the incursion of moisture from the Arabian Sea as it moved eastward from 22nd to 23rd January 2019. The high value of positive vorticity is gradually increased at upper troposphere (300–200 hPa) during the period and maximum vorticity (more than 5×10^{-5} s^{-1}) has been noticed at 00 UTC 22nd January. The intensity of the vorticity is slowly decreased as the system moved further eastward. The feature is plausibly well simulated in both the CTL (Fig. 7b) and RAD (Fig. 7c) experiments during the period. It is noted that the magnitude, time and spatial pattern of the high vorticity at the upper troposphere have been adequately simulated by the RAD (Fig. 7c), which is closely resembled with the ERA5 reanalyses. Conversely, these features are present in the CTL (Fig. 7b) simulation. Both the simulations considerably well predict the gradual decrease of vorticity. In Case 2, the high value of positive vorticity is observed around 300–200 hPa at 00 UTC 08th February 2019 in the ERA5 reanalyses (Fig. 7d) during the intensification of cyclonic circulation associated with the WD. It is noticed that the intensification of cyclonic circulation associated with the WD leads to the generation of high magnitude of vorticity in the RAD experiments (Fig. 7f) as compared to the CTL experiment (Fig. 7e). The intensity and spatial/temporal distribution of the vorticity from RAD simulation closely match with ERA5 (Fig. 7d). The magnitude of the vorticity
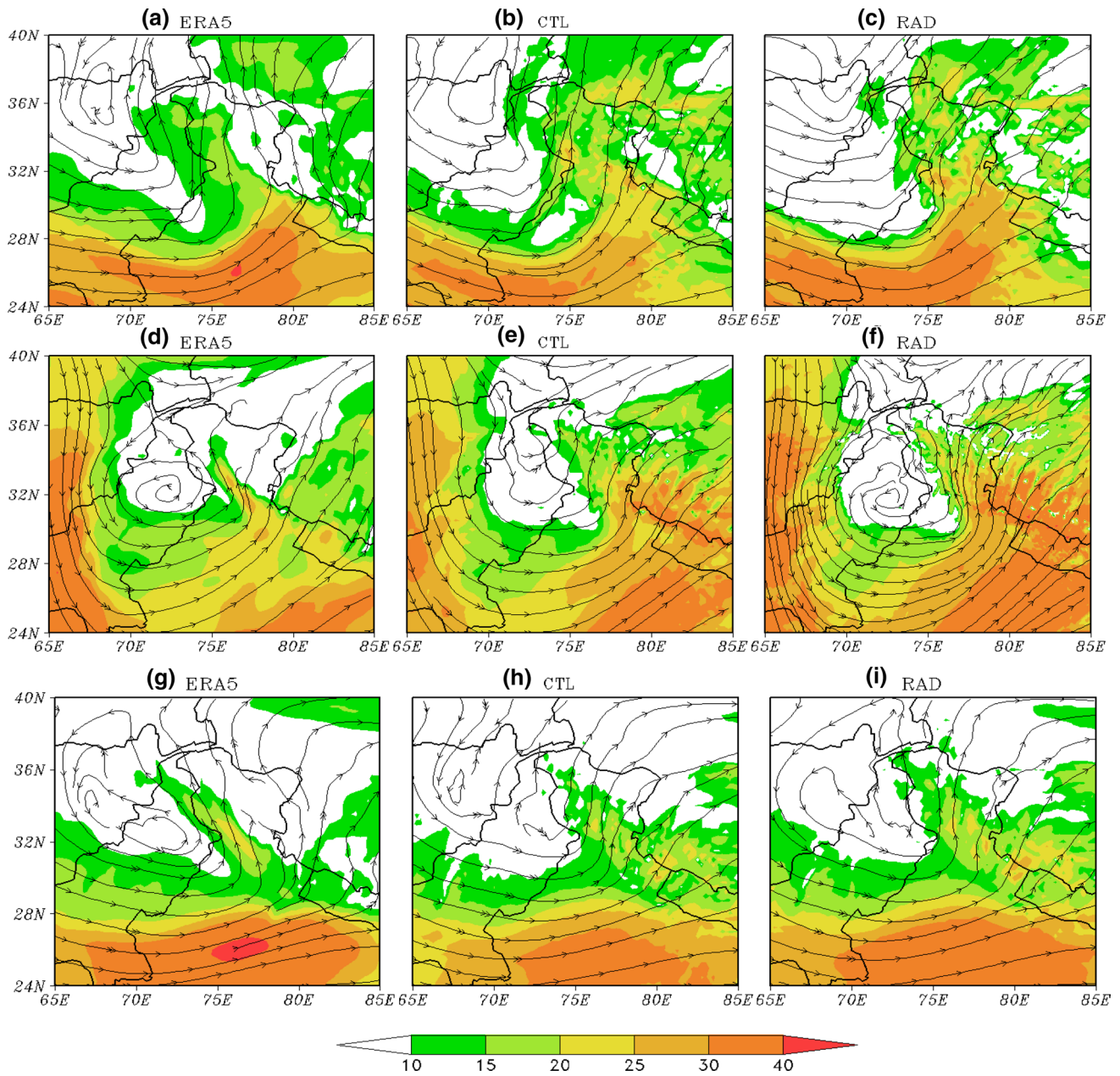
Fig. 6 Wind magnitude (m/s; shaded) and co-moving stream lines at 500 hPa for **a** ERA5; **b** CTL and **c** RAD of Case 1 valid at 00 UTC 22nd January 2019 (day-1 forecast). **d–f** and **g–i** are same as (**a–c**) but for Case 2 and Case 3 valid at 00 UTC 8th February 2019 and 29th January 2020, respectively

Table 4 RMSE of wind (m/s) at different pressure levels from model simulations calculated based on upper air observations (RS/RW)

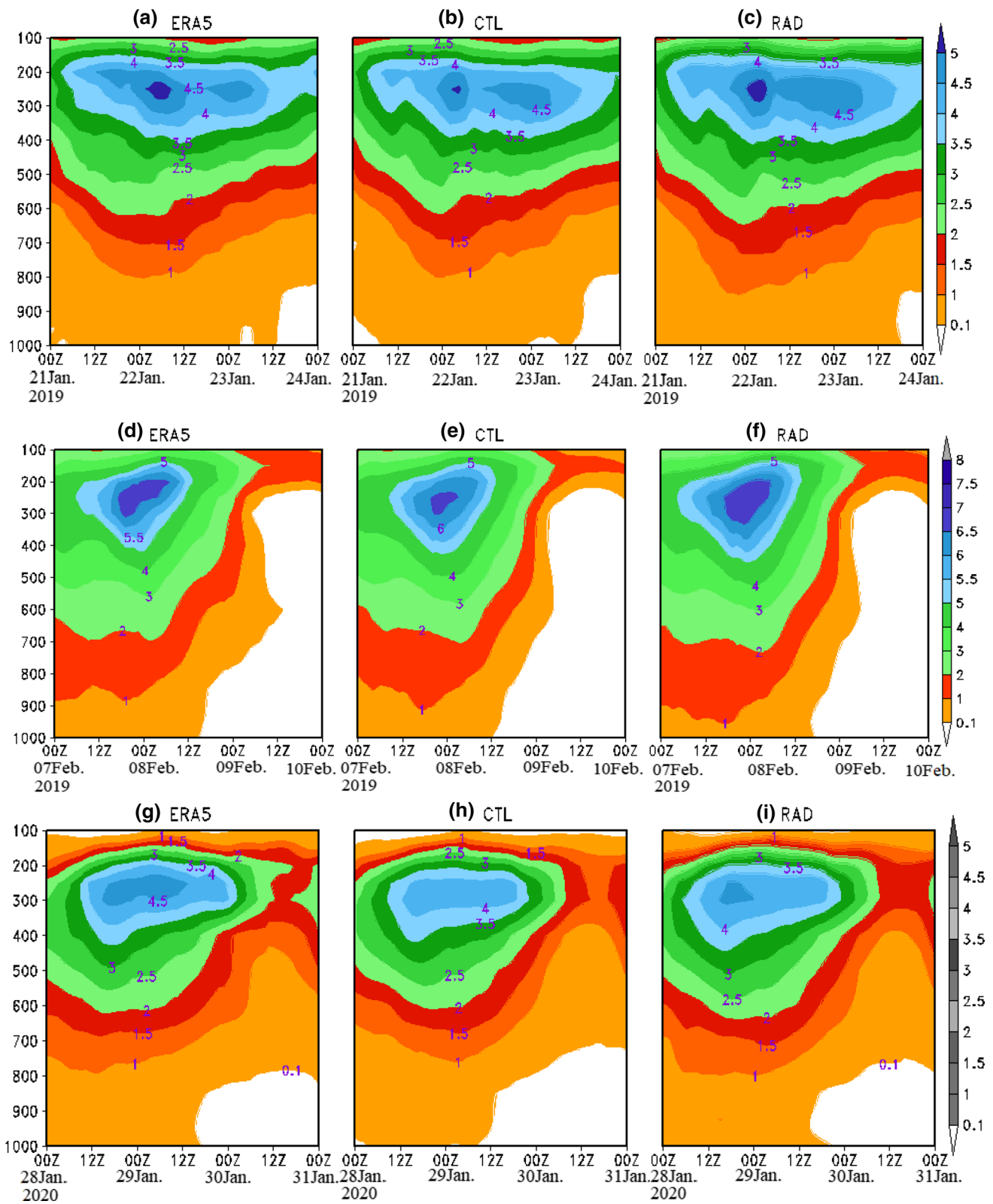| Pressure levels (hPa)	Case 1			Case 2			Case 3		
	CTL	RAD	Skill (%)	CTL	RAD	Skill (%)	CTL	RAD	Skill (%)
850	4.49	3.89	13.36	6.43	5.52	14.15	7.93	6.75	14.88
700	5.87	3.64	37.98	6.98	5.97	14.46	5.39	4.57	15.21
500	7.16	5.38	24.86	7.73	6.73	12.93	8.08	7.31	9.52
400	7.03	4.26	39.04	5.74	4.43	22.82	7.48	5.33	28.74
300	8.22	7.43	9.61	6.58	6.07	7.75	9.35	8.73	6.63

Fig. 7 Area averaged time-pressure cross-section of vorticity ($\times 10^{-5}$ s^{-1}) for **a** ERA5; **b** CTL and **c** RAD of Case 1. **d–f** and **g–i** are same as (**a–c**) but for Case 2 and Case 3, respectively. *Y*-axis: pressure levels (hPa)

is lower in the CTL simulation (Fig. 7e) during the study period. Similarly, for Case 3, the distribution of cyclonic vorticity is appropriately represented in the RAD (Fig. 7i), which is well correlated with the ERA5 reanalyses (Fig. 7g). It is necessary to mention here that one of the typical features associated with WD is the presence of a maximum of relative vorticity at 400–300 hPa or higher level similar to nascent extratropical cyclones or cases related to baroclinic instabilities (Robinson 1989; Davis 1992; Hunt et al. 2018c). Overall, the discrete pattern of vorticity associated with WD is well predicted by both the simulations. When a discreet comparison is made between CTL and RAD, it is deduced that the vorticity is well characterized after assimilation of radial velocity observations, which is closely matched with the reanalyses (ERA5) in all WD cases.

6.2.3 Rainfall

The 24 h accumulated precipitation from CTL and RAD simulations along with merged GPM satellite-rain gauge data for Case 1, Case 2 and Case 3 of day-1 are shown in Fig. 8a–c; d–f and g–i, respectively. In Case 1, the maximum quantity of precipitation was observed (Fig. 8a) over J&K, Himachal Pradesh, Punjab, Uttaranchal, Delhi and Utter Pradesh regions. The intensity and spatial distribution of precipitation over all the regions are clearly discernible in the RAD simulation (Fig. 8c) as seen in the observation (Fig. 8a). However, the areal distribution of precipitation is shifted more towards the north in the CTL simulation (Fig. 8b). It is also noticed that both the model simulations show wet bias over the region affected by WD compared to the rainfall observations. During the period, moderate rainfall of about 1–3 cm was observed over some parts of the south-southwest of the Rajasthan regions (Fig. 8a). The rainfall pattern over the region is better simulated by the RAD, whereas the simulated precipitation is slightly lower than the actual observation. Here, the CTL simulation could not be able to produce the belt of moderate precipitation over the same region as noticed in the observation. In Case 2, moderate to heavy rainfall with few areas of very heavy rainfall was observed over western Himalayan region during the period of study (Fig. 8d). It is noticed that both the model simulations (CTL and RAD) are able to produce the precipitation belt confined over the western Himalayan region. However, the precipitation belt simulated in the CTL (Fig. 8e) is closer to the foothill of the Himalayas than the observed pattern (Fig. 8d). Hence, the simulated locations of heavy to very heavy rainfall are considerably shifted northeastward in CTL. At the same time, the orientation of predicted rainfall over the region in RAD (Fig. 8f) is much closer to the observed pattern. The areal pattern of maximum rainfall (8–16 cm) is better simulated by the RAD, close to the observed distribution. Case 3 was a

weaker WD system, hence, light as well as scattered rainfall was observed (Fig. 8g) over western Himalayan regions. But both the model simulations (Fig. 8h and i) over-predicted the spatial distribution and amount of rainfall over the area during the WD period. From the 24 h accumulated rainfall, it is noticed that the model is able to estimate the heavier precipitation associated with the intense WD, whereas it overestimates during the lower rainfall event. This may be due to the high gradient of topography over the regions affected by WD, which plays a significant role in modulating the weather system, which may not be appropriately represented in the model. The study by Dimri (2004) indicates the proper representation of topography along with the finer resolution of the model, which further improved the forecast skill, particularly of the precipitation associated with the WDs over the northwest region. Topography plays a vital role in simulating the mesoscale features associated with the WD, which lead to heavy to very heavy precipitation over western Himalayan regions. It is necessary to point out that the model simulations shown the northeastward inclination and intense precipitation associated with the storm in all three cases, when compared with the observations. However, the northeastward shifting of the precipitation band related to the WDs and region of maximum precipitation is considerably improved with the use of radial velocity observations in the preparation of analysis. Overall, the model simulates the evolution and propagation of the WDs are reasonably well captured in the RAD.

The time series of radially averaged (250 km radius; considered Delhi DWR station Lat: 28.58° N and Long: 77.22° E as a centre point) 1-h accumulated model simulated rainrate (mm/hr) from CTL and RAD simulations (24 h) along with derived rainrate from Delhi DWR reflectivity for all the WD cases are depicted in Fig. 9a–c, respectively. It is clear from the figures that the rainfall pattern is well simulated in both experiments (CTL and RAD). But the intensity and variation pattern of the rainfall from RAD is closer to the DWR-derived hourly rainrate throughout the 24 h forecast period. In Case 1 (Fig. 9a), the DWR-derived rainrate shows maxima at 9–10 h and the rainfall spell continuously enhanced after 16 h. The RAD considerably well simulates the intensity of maxima and rapid increase of rainfall compared with the CTL. Hence, the RMSE and correlation (CC) are improved in the RAD simulation than that of CTL. In Case 2 (Fig. 9b), the observation shows a rapid increase of the rainrate during 11–18 h and maximum rainfall spell occurred at 18 h. The feature is well simulated by both the simulation, whereas the simulated maximum rainfall is early by 3 h and 1 h in the CTL and RAD experiments, respectively. The intensity and quick decrease of rainrate as seen in the observation are well featured in the RAD compared with the CTL. Similarly, the amount and pattern of the simulated rainfall in RAD is improved compared to the CTL in Case 3 (Fig. 9c). It is also
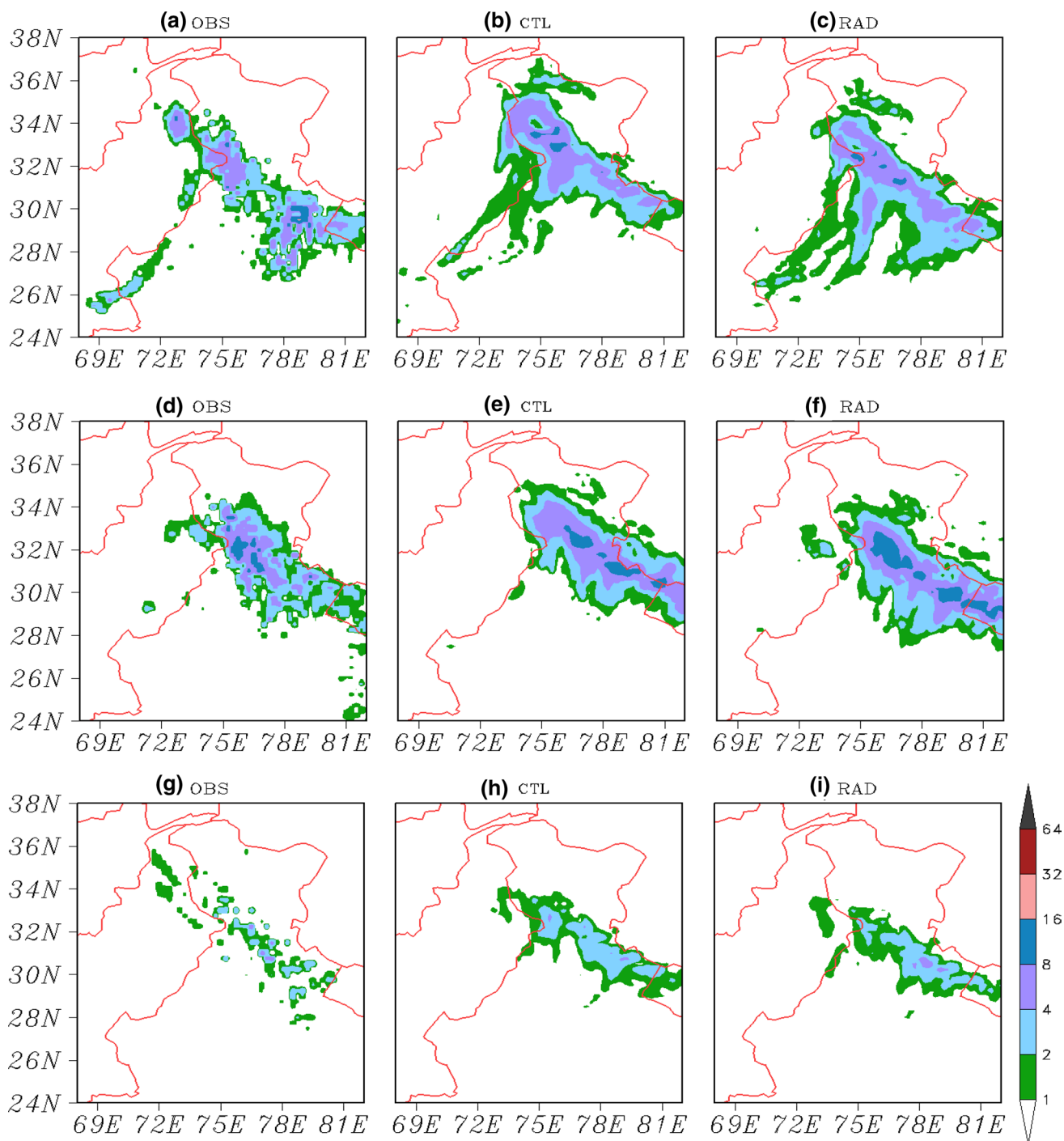
Fig. 8 24 h accumulated rainfall (cm) for **a** OBS; **b** CTL and **c** RAD of Case 1 valid at 00 UTC 22nd January 2019 (day-1). **d–f** and **g–i** are same as (**a–c**) but for Case 2 and Case 3 valid at 8th February 2019 and 29th January 2020, respectively

seen that the presence of maxima (minima) rainfall in the observation are considerably improved in RAD than that of CTL throughout forecast time. The RMSE (CC) from RAD experiment is also decreased (increased) with respect to the CTL. It is evident from the past studies that the forecast skill of rainfall associated with the extreme weather systems has been appreciably improved by assimilating the DWR radial wind along with other observations into the high-resolution regional models (Xiao et al. 2005; Routray et al. 2010, 2013; Prasad et al. 2014; Dutta et al. 2019; etc.).

The various statistical skill scores such as ETS, SAL and FSS from CTL and RAD simulations are calculated

Fig. 9 Hourly variation of radial averaged (250 km) of rainfall up to 24 h from DWR (Delhi); CTL and RAD simulations for **a** Case 1; **b** Case 2 and **c** Case 3
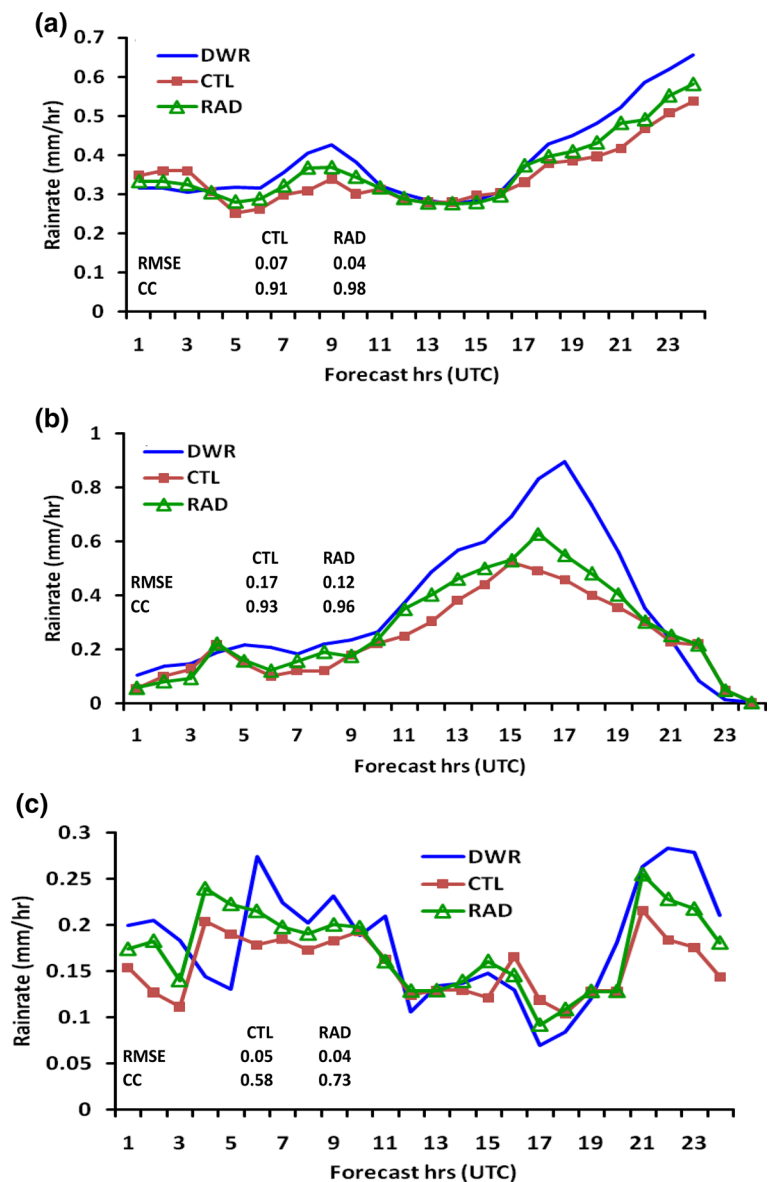
for the day-1 forecast with respect to the NCMRWF-IMD rainfall analysis over the region of 24°–38° N; 68°–82° E. Figure 10a, b describes the ETS along with % improvement at different rainfall thresholds (mm) for Case 1 and Case 2, respectively. It is seen from the figures that the values of ETS at different rainfall thresholds are more after the assimilation of the DWR radial winds than the CTL simulation in both cases. The values of ETS are gradually decreased with the increase of rainfall thresholds in all the cases. But it is noted that the RAD simulations give higher ETS values than the CTL simulation. The % of improvement of RAD is relatively higher with respect to the CTL simulation at various thresholds in both cases. It is observed that the gain skill is found higher at lower thresholds (up to 15 mm) and the skill steadily reduced as the thresholds increase during the period in all the cases. The average gain skill of about

34% and 28% is seen in the RAD simulation for Case 1 and Case 2, respectively.

The performance of the model precipitation forecasts is evaluated over a pre-specified domain through a novel object-based quality measure called Structure-Amplitude-Location (SAL; Wernli et al. 2008). Figure 10c, d depicts the three components of SAL along with gain skill for Case 1 and Case 2, respectively. All components of the SAL from both cases indicate that the model overestimated the precipitation during the study period. However, the values of the SAL from all the three components are reduced considerably in RAD compared to the CTL 24 h simulations. The structure component of SAL is fairly small in both simulations. This is mainly due to proper simulation of the spatial distribution of the rainfall by the model over the specified domain (Fig. 8a–f). But the S-component is improved by 22% and
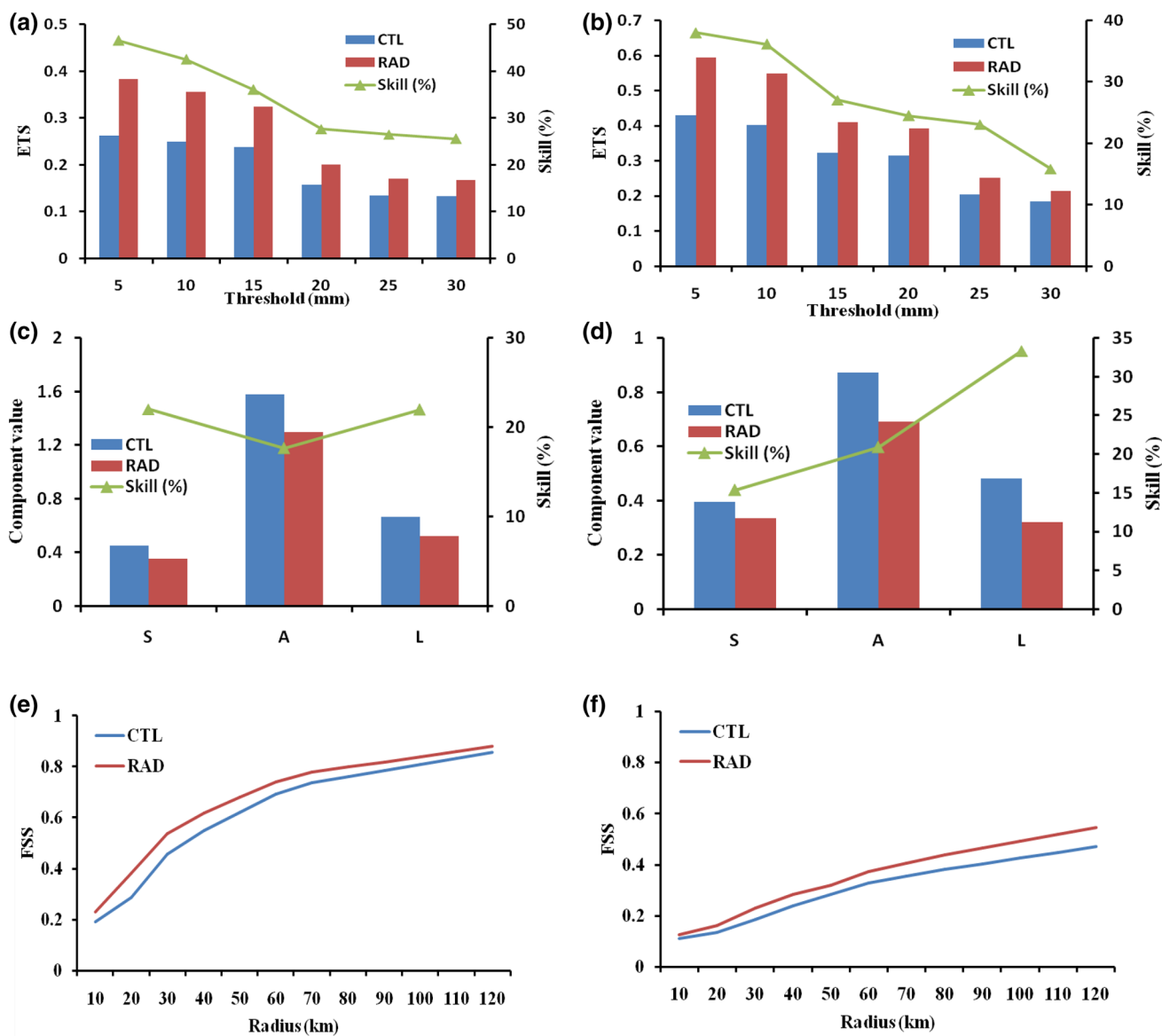
Fig. 10 Equitable threat score (ETS) at different rainfall thresholds (mm) along with % of improvement of RAD over CTL (line in right-hand *Y*-axis) of day 1 (24 h) for **a** Case 1 and **b** Case 2. Structure-Amplitude-Location (SAL) of day 1 (24 h) for **c** Case 1 and **d** Case 2. **e**, **f** are same as (**c**, **d**) but for Fractions Skill Score (FSS) at 10-mm rainfall threshold, respectively

15% in the RAD simulation compared to the CTL for Case 1 and Case 2, respectively. A large amount of error occurred in terms of A-component of SAL in both cases mainly due to the overestimation of the rainfall along the foothill of the Himalayan region as compared to the observations during the period (Fig. 8). The values of A-component are relatively less in the RAD with the gain skill of 18% and 21% over the CTL simulations for Case 1 and Case 2, respectively. The location error is reasonably small compared with the amplitude component's error in all cases. The positive value of the L-component indicates that the model simulation cannot capture the spatial distribution of the objects relative to the center of mass or shift of rainfall areas in the forecast.

Typically, the CTL simulations (Fig. 8b and e) show the northeastward shift of the precipitation areas compared to the observations. It is clearly seen that the northeastward shift of rainfall belts is considerably reduced in RAD simulations. Hence, the positive value of the L-component is significantly reduced in RAD simulation. The % of improvement is noticed by 22% and 33% in the RAD compared to CTL in Case 1 and Case 2, respectively. In Case 3, it is seen that the precipitation is not perfectly brought out in the model simulations as indicated by the largest errors in S, A and L components, the figure is not given here due to brevity. The model simulates precipitation over a large area, with intense rainfall over northwest Indian regions (Fig. 8h,

i), while the observation has scatter rainfall over the region. Therefore, all three components of SAL are largest positive values, suggesting an overestimation of the total rainfall and northeastward shift of the precipitation area, mainly in the CTL, over the domain. But the positive values of all components of SAL are slightly reduced in the RAD simulation than the CTL simulation.

Figure 10e, f represents the FSS at the 10 mm threshold of rainfall for Case 1 and Case 2, respectively. The figures clearly show that the model does not precisely predict the observed rainfall intensity. However, the FSS values are relatively improved in the RAD simulation for all the cases as compared to the CTL. Unlike Case 1 (Fig. 10e), the value of FSS is increased with the increase of radius of influence in Case 2 (Fig. 10f). But the values of FSS are less in Case 2 as compared to Case 1 during the period of study. It is difficult to find out any meaningful information on the spatial accuracy of the model from these figures. Hence, we further evaluated the impact of assimilation of the DWR radial velocity on simulation of precipitation associated with the WDs by comparing the 24 h accumulated model simulated rainfall with the observed station values reported by IMD over northwest regions (Table 5). In Case 1, the maximum rainfall (9 cm) over few stations (Table 5) during day-1 is not exactly captured by both model simulations. However, the RAD simulated precipitation over these stations is noticeably improved and closer to the observations as compared to the CTL simulation. From Table 5, it is clearly noticed that the simulated amount of precipitation from the RAD is closely matched with the observed amount of precipitation at many stations than that of CTL in all the cases.

6.2.4 Kinetic energy (KE) budget

The time-pressure cross-section of the horizontal flux of KE from the verification reanalyses (ERA5) along with the 72 h model simulations (CTL and RAD) for Case 1 is depicted in Fig. 11a during the period 00 UTC of 21st to 24th January 2019. In the ERA5, it is observed that convergence of horizontal flux of KE is extended from the surface to 500 hPa. The maximum convergence of flux ($\sim -5 \times 10^{-4}$ W kg^{-1}) is located at 700–500 hPa level during the period 00 UTC of 21 to 18 UTC of 22 January, where the WD was intensified as per the IMD report. The high convergent magnitudes in the vicinity of the low-pressure centre decreased later as the system moved eastward and WD weakened. There is an increase of divergent flux of KE above the 500 hPa level due to the rise of pressure and decreasing of the pressure gradient. But at 300 hPa, the divergence flux of KE is sharply increased, it may vary between 20 and 25 ($\times 10^{-4}$ W kg^{-1}) units. One can say, the significant changes in the horizontal flux of KE that occur in the upper troposphere are probably due to the presence of the subtropical jet stream. Both the experiments

Table 5 Comparison between model simulated and station-wise observed precipitation (cm) for day-1

Station names	Lat. (°)	Lon. (°)	OBS	CTL	RAD
Case 1 valid at 03 UTC 22 January 2019					
Pathankot	32.27	75.65	9	5.2	7.1
Batote	33.12	75.32	9	6.3	7.4
Bharwain	31.79	76.12	9	6.1	7.5
Nagina	29.44	78.43	7	3.1	6.6
Mukerian	31.95	75.61	7	4.8	5.5
Ghamroor	31.95	75.95	6	3.7	5.9
Adampur	31.43	75.71	6	4.5	5.7
Dharamshala	32.21	76.32	5	7.4	4.9
Ludhiana	30.90	75.85	5	2.73	3.4
Ranikhet	29.64	79.43	4	2.6	3.6
Dharchula	29.84	80.53	4	2.4	3.7
Srinagar	34.08	74.79	3	2.0	2.7
Case 2 valid at 03 UTC 08 February 2019					
Hoshiarpur	31.51	75.91	8	3.9	5.8
Gulmarg	34.04	74.38	7	4.9	5.6
Srinagar	34.08	74.79	5	2.6	3.3
Baderwah	32.98	75.71	5	7.3	5.6
Naina Davi	31.30	76.53	5	1.7	3.8
Phagwara	31.22	75.76	4	1.9	3.9
Udhampur	32.91	75.14	4	7.0	3.3
Katra	32.99	74.93	4	5.9	3.2
Nangal	31.38	76.37	4	3.2	3.5
Jammu City	32.72	74.85	3	4.2	2.1
Pathankot	32.27	75.65	3	4.2	3.5
Baldwara	31.55	76.76	3	5.5	4.4
Kaiserganj	27.25	81.54	3	1.8	4.2
Samana	30.15	76.19	3	0.78	2.6
Case 3 valid at 03 UTC 29 January 2020					
Solan	30.90	77.09	6	3.1	3.4
Palampur	32.11	76.53	5	4.3	4.6
Khadrala	31.20	77.75	5	6.4	7.2
Kufri	31.09	77.26	5	5.4	4.8
Dharmasala	32.21	76.32	5	4.1	5.5
Pachhad	32.08	77.57	4	4.3	4.1
Jatton Barrage	30.56	77.47	4	3.7	4.1
Shimla	31.10	77.17	4	4.7	4.3
Gairsain	30.05	79.28	4	2.8	4.9
Dharchula	29.84	80.53	3	2.3	3.1
Manali	32.24	77.18	3	6.2	5

reasonably well simulate the vertical and temporal distributions of the flux. The magnitude and spatial variation of flux convergence at the mid-troposphere are considerably well simulated in the RAD than in the CTL simulation. Similarly, the spatial pattern and magnitude of divergent flux are also well simulated in the RAD. The vertical distribution and magnitude of the flux from RAD simulation are closely
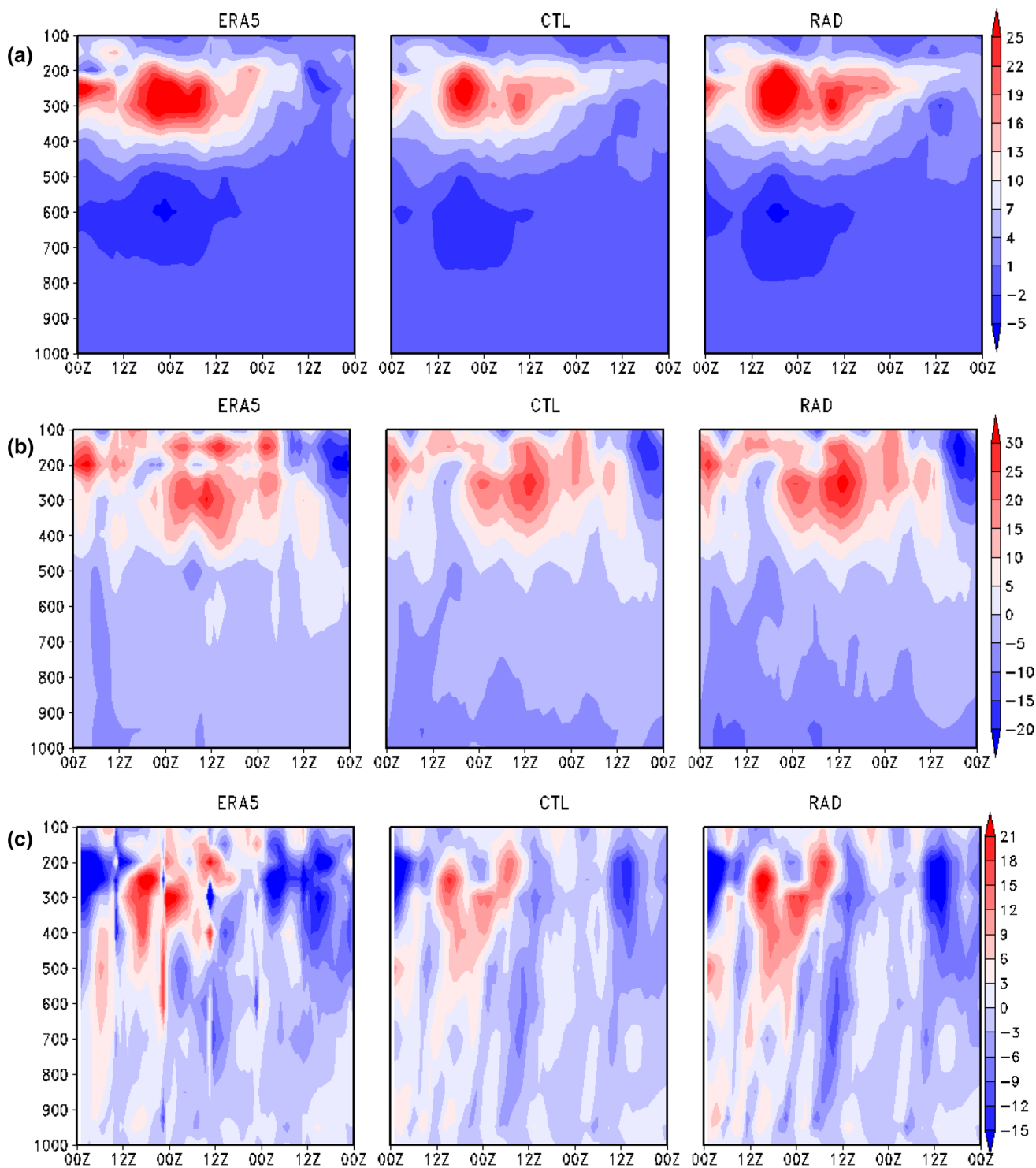
Fig. 11 Time-pressure cross-section of **a** Horizontal flux of KE ($\vec{\nabla}.K\vec{V}$; W kg^{-1}); **b** Adiabatic generation of KE ($-\vec{V}.\nabla\varphi$; W kg^{-1}) and **c** Change of KE ($\frac{\partial K}{\partial t}$; J m^{-2}) from ERA5 reanalysis, CTL and RAD experiments for the period 00 UTC 21st to 24th January 2019 of Case 1. Y-axis: pressure levels (hPa)

matching with the ERA5 reanalysis. Figure 11b illustrates time-pressure cross-section of the adiabatic generation of KE from ERA5 reanalysis, CTL and RAD simulations during the period 00 UTC of 21st to 24 January 2019 for the WD (Case 1). In the ERA5, it is observed that weak magnitudes of dissipation of KE take place up to 500 hPa

height from the surface in WD. The positive magnitude of adiabatic generation of KE is noticed in the upper levels. The generation of KE slowly increased during the initial phase of the WD and achieved the maximum magnitude during the intense phase of the WD (00 UTC 22 to 23 January 2019). Subsequently, the positive magnitude of adiabatic generation of KE gradually decreased as well as the appearance of dissipation of KE is noticed when the system moved further eastward. The magnitude, evolution and propagation of generation of KE are well simulated by the RAD as compared to the CTL. The features are well correlated with the corresponding ERA5 reanalyses. However, the dissipation of KE is slightly higher predicted by both the simulations at lower atmosphere during the period when compared with the verification analysis. The time-pressure cross-section of the tendency of KE term from ERA5 reanalyses, CTL and RAD simulations during the period 00 UTC of 21st to 24 January 2019 (for the Case 1 WD) is demonstrated in Fig. 11c. The negative and subsequent positive values of the tendency of KE are observed in ERA5, it represents like ridge and trough pattern in KE tendency. The positive tendency of KE is noticed during the intense phase of the WD, extended from mid to upper atmospheric levels and found to be maximum at 400–200 hPa. The positive tendency gradually deteriorated when the system advanced further eastward. The RAD forecast shows similar magnitude and distribution of KE tendency similar to ERA5. The magnitude of KE's tendency is underestimated in the CTL forecast compared to ERA5 reanalyses. It is observed that horizontal flux and adiabatic generation of KE are the two equally important sources of generation of KE during the WD.

The various terms of the KE budget are depicted in Fig. 12a–c, for Case 1 and Case 2, respectively. In ERA5 (Fig. 12a), the convergent magnitude is about -2 to -5×10^{-4} W kg^{-1} around the vicinity of the low-pressure system and increased within the centre of the WD during the period 00 UTC 7 to 8 February 2019. There is an increase of divergent flux of KE at upper levels during the same period. It may be possible that the high divergent flux of KE is associated with the steepest pressure gradient between the mid- and upper atmosphere during the WD. It is seen that the convergent flux at upper level starts appearing after 06 UTC of 7th February 2019, probably due to the dominance of the tropical easterly jet stream. Both experiments well simulated the features, but the magnitude and distribution pattern of flux slightly improved in RAD simulation. Figure 12b illustrates the adiabatic generation of KE obtained from ERA5 and two experiments for Case 2. It is seen from ERA5, the magnitudes of dissipation of KE are obtained during the initial phase of the WD. The generation of KE is gradually increased from 500 hPa and extended up to the upper atmospheric levels after 00 UTC of 8th February 2019, in which the system was progressively intensified due to pumping of high moisture from the Arabian Sea, strong wind confluence at lower levels and divergence at upper troposphere during 8th and 9th February 2019 (as per the IMD weather report). The dissipation and generation of the KE are relatively well simulated in the RAD than that of the CTL. The features are well comparable with the corresponding ERA5 reanalyses. The tendency of KE (Fig. 12c) of Case 2 has a similar distribution pattern to Case 1. The structure and evolution of the KE tendency in the RAD simulation throughout the forecast period are in comparison with CTL and is closely matching with the ERA5 reanalyses.

7 Summary and conclusions

The present study evaluated the impact of assimilation of DWR radial velocity in the high-resolution regional NCUM analysis-forecast system by simulating three WDs that produced an enormous amount of precipitation over northwest regions. To fulfill the objective of the present study, we conducted two numerical experiments named as CTL (assimilation of a variety of conventional and non-conventional observations obtain at NCMRWF) and RAD (assimilated DWR radial velocity plus other observations used in CTL). The initial conditions for NCUM-R forecast model is prepared through 4DVAR data assimilation system. Some of the significant findings from the current study are summarized below:

- The model analyses captured the spatial distribution of 500 hPa wind and geopotential height fields associated with the WDs reasonably well as compared to the ERA5 reanalysis used for the verification. It is noticed that the CTL analyses produced intense magnitude of wind, mainly over western Himalayan regions in all the cases compared to ERA5 reanalyses.
- The intense wind patterns over the regions are corrected in the RAD analyses significantly with the assimilation of the DWR radial wind in all the cases. However, some underestimation is also observed in the wind magnitude over the certain pocket of northwest regions in the RAD analyses. The RMSE of wind components are noticeably reduced in the RAD analyses than CTL analyses for all cases.
- The south-westerly bias over the western Himalayan region observed in CTL analyses in all the WD cases. This intense positive bias in the analysis may be due to the scarcity of surface and upper-air observations over and along the steep Himalayan regions. Assimilation of radial velocity improved the analyses that properly characterized the intensity and wind pattern associated with WD cases, which compensated the dearth of wind observations over the mountainous regions on certain extent.
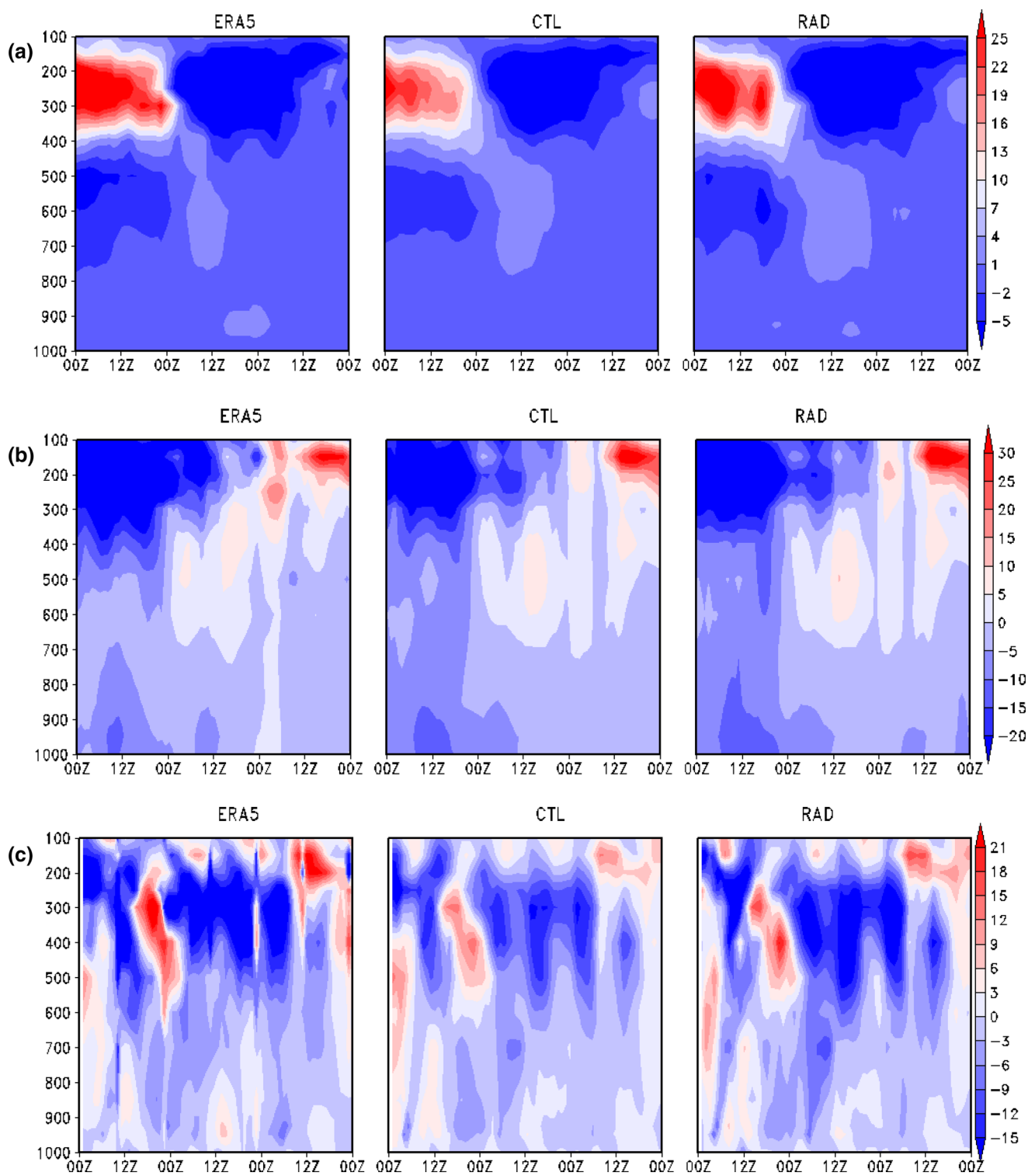
Fig. 12 Same as Fig. 11 but for Case 2 during the period 00 UTC 7th to 10th February 2019. *Y*-axis: pressure levels (hPa)

- The RAD analyses are well manifested in the northward transport of moisture fluxes from the Arabian Sea and spatial distribution of moisture convergence zone around the cyclonic circulation, which is closely matched with the ERA5 reanalyses in all the cases. But the strong magnitude of moisture fluxes is noticed in the CTL analyses on many occasions over the domain.

- The day 1 (24 h) wind simulations clearly suggested that the spatial distribution of wind associated with the WDs is reasonably well characterized in the RAD after the assimilation of the radar radial velocity compared to the CTL simulation. The features are comparable with ERA5 as well as IMD analyzed wind fields.

- The RMSEs of wind speed at various pressure levels are noticeably reduced in the RAD simulations than that of CTL simulations in all the cases. The mean RMSE for Case 1–3 is reduced by 25%, 14% and 15% in the RAD simulation with respect to CTL simulation, respectively. The findings i.e., the wind RMSE considerably reduced after assimilation of the radial wind is well supported by other earlier studies (Abhilash et al. 2007; Routray et al. 2013; Prasad et al. 2014; Dutta et al. 2019; etc.).

- The central maximum of relative vorticity is observed at 400–300 hPa or higher level is one of the major characteristics associated with the WDs (Robinson 1989; Davis, 1992; Hunt et al. 2018c). The increase of positive vorticity throughout the atmosphere and maximum at the upper troposphere (300–200 hPa) is predicted by both the simulations during the intense phase of the WDs and the intensity of the positive vorticity slowly decreased when the system moves further eastward. It is noted that the magnitude, time and spatial pattern of the high vorticity at the upper troposphere are adequately well simulated by the RAD and is matching well with the ERA5 reanalyses in all cases.

- It is noticed that the CTL simulated precipitation belt is positioned more northeastward, close to the foothill of Himalaya, compared to observations in all cases. However, the distribution pattern of rain band associated with the WDs and region of maximum precipitation is considerably improved in the RAD simulations.

- Overall the various statistical skill scores revealed that the assimilation of radar radial velocity observation into the high-resolution assimilation-forecast system improved the rainfall simulation reasonably well over northwest regions during the passage of WDs.

- The magnitude, evolution and propagation of various KE budget terms are relatively well simulated in the RAD than the CTL and the features are closely matched with the ERA5 reanalyses in all the WD cases.

- The results obtained from the present study firmly indicate that the assimilation of the high spatial/temporal quality of DWR radial winds in the analysis system has a positive impact on the simulation of the evolution and propagation of WD and associated precipitation. The DWR radial wind observation reduced the scarcity of wind observations over the regions we considered for the study.

- However, it is noticed that model could not simulated the precipitation associated with the WDs very well everywhere and many instant the results are not encouraging after assimilation of the DWR radial velocity. The issue in this study is that only Patiala DWR station (VICH) observations are assimilated (Fig. 2d and e) in the assimilation cyclic. The Srinagar (VISR) DWR observations were missing in the Case 1 and Case 2 and only minimal observations available for Case 3 (Fig. 2f). Hence, very less amount of observations is available for assimilation cyclic.

- The maximum DWR observations are also discarded (attenuation) through quality control check due to the steep and intricate orography of the Himalayan ranges. Therefore, the forecast skill of model is not encouraging over the region as compared to the impact studies of assimilation of DWR data by simulating different weather systems affected over other regions (Osuri et al. 2015; Routray et al. 2010, 2013; Dutta et al. 2019; etc.).

- The model results vary over the region due to non-uniformity of the terrain as well as diverse in the land-use/land-cover patterns (Dimri and Chevuturi 2014; Thomas et al. 2014, 2018; etc.). Much more research effort is required for the further improvement of the model forecast skill.

Author contributions DD: conducting experiments, visualization, software; AR: conceptualization, methodology, writing—original draft preparation; AL: data curation, software, investigation; JPG: supervision, writing—reviewing and editing; AKM: supervised the overall work, provided infrastructure facilities.

Data availability statements The datasets generated during and/or analyzed during the current study are available from the corresponding author on reasonable request.

Availability of data and materials The data and the materials used in the study are collected from the publicly (free) and internal available repositories. (1) Fifth generation ECMWF reanalyses (ERA5) dataset are used for verification purpose are available from https://cds.climate.copernicus.eu/cdsapp#!/dataset/reanalysis-era5-pressure-levels?tab=overview (2) IMD-NCMRWF Global Precipitation Measurement (GPM) satellite-rain gauge merged rainfall used as observation is available https://www.imdpune.gov.in/Clim_Pred_LRF_New/Grided_Data_Download.html. (3) Upper air chart of streamline analyses is available in https://www.imdpune.gov.in/Clim_Pred_LRF_New/. (4) Doppler Weather Radar (DWR) and satellite observations: From NCMRWF and IMD Internal repositories.

Code availability The NCUM-R forecast modeling system is a licensed version of UK Met office Unified Model (UM). The source code is available within the UM partnership.

Declarations

Conflict of interest The authors declare that there are no conflicts of interest/competing interests for this research work.

References

Abhilash S, Das S, Kalsi SR, Das Gupta M, Mohan Kumar K, George JP, Banerjee SK, Thampi SB, Pradhan D (2007) Impact of doppler radar wind in simulating the intensity and propagation of rainbands associated with mesoscale convective complexes using MM5-3DVAR system. Pure Appl Geophys 164:1491–1509

Anagnostou EN, Krajewski WF (1999) Real-time radar rainfall estimation. Part I: algorithm formulation. J Atmos Ocean Tech 16:189–197. https://doi.org/10.1175/1520-0426(1999)016%3c0189:RTRREP%3e2.0.CO;2

Azadi M, Mohanty UC, Madan OP, Padmanabhamurty B (2001) Prediction of precipitation associated with western disturbances using a high-resolution regional model: role of parameterization of physical processes. Meteorol Appl 7:317–326

Ballard SP, Li Z, Simonin D, Caron J-F (2016) Performance of 4D-Var NWP based nowcasting of precipitation at the Met Office for summer 2012. Q J R Meteorol Soc 142:472–487

Clark DB, Mercado LM, Sitch S, Jones CD, Gedney N, Best MJ, Pryor M, Rooney GG, Essery RLH, Blyth E, Boucher O (2011) The joint UK land environment simulator (JULES), model description–Part 2: carbon fluxes and vegetation dynamics. Geosci Model Dev 4(3):701–722

Cullen MJP, Davies T, Mawson MHJ, James A, Coulter SC, Malcolm A (1997) An overview of numerical methods for the next generation U.K. NWP and climate model. Atmos Ocean 35:425–444

Davies T, Cullen MJP, Malcolm AJ, Mawson MH, Staniforth A, White AA, Wood N (2005) A new dynamical core for the Met Office's global and regional modeling of the atmosphere. Q J R Meteorol Soc 131:1759–1782

Davis CA (1992) A potential-vorticity diagnosis of the importance of initial structure and condensational heating in observed extratropical cyclogenesis. Mon Weather Rev 120:2409–2428

Dimri AP (2004) Impact of horizontal model resolution and orography on the simulation of a western disturbance and its associated precipitation. Meteorol Appl 11:115–127

Dimri AP (2007) The transport of momentum, sensible heat, potential energy and moisture over the western Himalayas during the winter season. Theor Appl Clim 90:49–63

Dimri AP (2012) Atmospheric water budget over the western Himalayas in a regional climate model. J Earth Syst Sci 121:963–973

Dimri AP, Chevuturi A (2014) Model sensitivity analysis study for western disturbances over the Himalayas. Meteorol Atmos Phys 123:155–180

Dimri AP, Mohanty UC (2009) Simulation of mesoscale features associated with intense western disturbances over western Himalayas. Meteorol Appl 16:289–308

Dimri AP, Niyogi D (2013) Regional climate model application at subgrid scale on Indian winter monsoon over the western Himalayas. Int J Climatol 33(9):2185–2205

Dimri AP, Mohanty UC, Mandal M (2004) Simulation of heavy precipitation associated with an intense western disturbance over Western Himalayas. Nat Hazards 31:499–552

Dutta D, Sharma S, Sen GK, Kannan BAM, Venketswarlu S, Gairola RM, Das J, Viswanathan G (2011) An Artificial Neural Network based approach for estimation of rain intensity from spectral moments of a Doppler Weather Radar. Adv Space Res 47:1949–1957

Dutta D, Kasimahanthi AJ, Devarajan PK, George JP, Rajagopal EN (2016) Winter hailstorms signatures by C-band polarimetric radar at Delhi. J Appl Remote Sens 10:026022

Dutta D, Kasimahanthi AJ, MallickS GJP, Devarajan PK (2017) Quality assessment of VVP winds from Indian Doppler weather radars: a data assimilation perspective. J Appl Remote Sens 11(3):036021

Dutta D, Routray A, Preveen Kumar D, George JP, Singh V (2018) Simulation of a heavy rainfall event during southwest monsoon using high-resolution NCUM-modeling system: a case study. Meteorol Atmos Phys 131:1035–1054

Dutta D, Routray A, Preveen Kumar D, George JP (2019) Regional data assimilation with the NCMRWF unified model (NCUM): impact of doppler weather radar radial wind. Pure Appl Geophys 176:4575–4597

Ebert E (2008) Fuzzy verification of high-resolution gridded forecasts: a review and proposed framework. Meterological Applications 15:51–64

Ebert E (2009) Neighborhood verification: a strategy for rewarding close forecasts. Weather Forecast 24:1498–1510

Gao J, Xue M, Shapiro A, Droegemeier KK (1999) A variational method for the analysis of three-dimensional wind fields from two Doppler radars. Mon Weather Rev 127:2128–2142

Hatwar HR, Yadav BP, Rao YVR (2005) Prediction of western disturbances and associated weather over Western Himalaya. Curr Sci 88:913–920

Hunt KMR, Curio J, Turner AG, Schiemann R (2018a) Subtropical westerly jet influence on the occurrence of western disturbances and Tibetan Plateau vortices. Geophys Res Lett 45:8629–8636. https://doi.org/10.1029/2018GL077734

Hunt KMR, Turner AG, Shaffrey LC (2018b) Extreme daily rainfall in Pakistan and north India: Scale interactions, mechanisms, and precursors. Mon Wea Rev 146:1005–1022

Hunt KMR, Turner AG, Shaffrey LC (2018c) The evolution, seasonality, and impacts of western disturbances. Q J R Meteor Soc 144:278–290

Kasimahanthi A, Dutta D, Devarajan PK, George JP, Rajagopal EN (2017) Quality characterization of reflectivity and radial velocity observed by Indian Doppler weather radars. J Appl Remote Sens 11(3):036026

Kung EC, Baker WE (1975) Energy transformations in middle latitudes. Q J R Meteorol Soc 101:793–815

Lang TJ, Barros AP (2004) Winter storms in the central Himalayas. J Meteorol Soc Jpn 82:829–844

Lawson JR, Gallus WA Jr (2016) Adapting the SAL method to evaluate reflectivity forecasts of summer precipitation in the central United States. Atmos Sci Lett 17:524–530

Lock AP, Brown AR, Bush MR, Martin GM, Smith RNB (2000) A new boundary layer mixing scheme. Part I: Scheme description and single-column model tests. Mon Weather Rev 128:3187–3199

Marshall JS, McK Palmer W (1948) The distribution of raindrops with size. J Meteorol 5:165–166

Mitra AK, Bohra AK, Rajeevan MN, Krishnamurti TN (2009) Daily Indian precipitation analyses formed from a merged of rain-gauge with TRMM TMPA satellite derived rainfall estimates. J Met Soc Japan 87(A):265–279

Mohanty UC, Pattanayak S, Litta AJ, Routray A, Kishore OK (2011) Simulation of heavy rainfall in association with extreme weather events: Impact on agriculture. In: Challenges and opportunities in agrometeorology, pp 35–59

Osuri KK, Mohanty UC, Routray A, Mohapatra M (2012) The impact of satellite derived wind data assimilation on track, intensity

and structure of tropical cyclones over North Indian Ocean. Int J Remote Sens 33:1627–1652

Osuri KK, Mohanty UC, Routray A, Niyogi D (2015) Improved prediction of Bay of Bengal tropical cyclones through assimilation of Doppler weather radar observations. Mon Weather Rev 143(11):4533–4560

Pant GB, Rupa Kumar K (1997) Climates of South Asia, John Wiley and Sons, Chichester, UK, 1997, pp XXIII + 320, ISBN 0-471-94948-5

Patil R, Kumar PP (2016) WRF model sensitivity for simulating intense western disturbances over North West India. Model Earth Syst Environ 2:82

Prasad SK, Mohanty UC, Routray A, Osuri KK, Ramakrishna S, Niyogi D (2014) Impact of Doppler weather radar data on thunderstorm simulation during STORM pilot phase—2009. Nat Hazards 74:1403–1427

Raju PVS, Bhatla R, Mohanty UC (2011) A study on certain aspects of kinetic energy associated with western disturbances over northwest India. Atmósfera 24(4):375–384

Rakesh V, Singh R, Yuliya D, Pal PK, Joshi PC (2009) Impact of variational assimilation of MODIS thermodynamic profiles in the simulation of western disturbance. Int J Remote Sens 30:4867–4887

Rawlins F, Ballard SP, Bovis KJ, Clayton AM, Li D, Inverarity GW, Lorenc AC, Payne TJ (2007) The Met Office global four-dimensional data assimilation system. Q J R Meteorol Soc 133:347–362

Roberts N, Lean H (2008) Scale-selective verification of rainfall accumulations from high-resolution forecasts of convective events. Mon Weather Rev 136:78–97

Robinson WA (1989) On the structure of potential vorticity in baroclinic instability. Tellus A 41:275–284

Routray A, Mohanty UC, Rizvi SRH, Niyogi D, Osuri KK, Pradhan D (2010) Impact of Doppler weather radar data on numerical forecast of Indian monsoon depressions. Q J R Meteorol Soc 136:1836–1850

Routray A, Mohanty UC, Osuri KK, Kiran Prasad S (2013) Improvement of monsoon depressions forecast with assimilation of Indian DWR data using WRF-3DVAR analysis system. Pure Appl Geophys 170:2329–2350

Routray A, Mohanty UC, Osuri KK, Kar SC, Niyogi D (2016) Impact of satellite radiance data on simulations of Bay of Bengal tropical cyclones using the WRF-3DVAR modeling system. IEEE Trans Geosci Remote Sens 54(4):2285–2303

Routray A, Abhishek L, Dutta D, George JP (2020) Study of an Extremely Severe Cyclonic Storm "Fani" over Bay of Bengal using regional NCUM modeling system: a case study. J Hydrol 590:125357

Routray A, Dutta D, Abhishek L, George JP (2021) Impact of the assimilation of DWR-derived precipitation rates through latent heat nudging on simulation of rainfall events over Indian region using NCUM-R. J Hydrol 596:26072

Stewart LM, Dance SL, Nichols NK (2008) Correlated observation errors in data assimilation. Int J Numer Methods Fluids 58:1521–1527

Thomas L, Dash SK, Mohanty UC (2014) Influence of various land surface parameterization schemes on the simulation of western disturbances. Meteor Appl 21:635–643

Thomas L, Dash SK, Mohanty UC, Babu CA (2018) Features of western disturbances simulated over north India using different land-use data sets. Meteor Appl 25:246–253

Vaidya SS, Mukhopadhyay P, Trivedi DK, Sanjay J, Singh SS (2004) Prediction of tropical systems over Indian region using mesoscale model. Meteorol Atmos Phys 86:63–72

Wernli H, Paulat M, Hagen M, Frei C (2008) SAL—a novel quality measure for the verification of quantitative precipitation forecasts. Mon Weather Rev 136(11):4470–4487

Wernli H, Hofmann C, Zimmer M (2009) Spatial forecast verification methods intercomparison project: application of the SAL technique. Weather Forecast 24(6):1472–1484

Wilson RW, Ballard SP (1999) A micro physically based precipitation scheme for the UK Meteorological Office Unified Model. Q J R Meteorol Soc 125:1607–1636

Xiao Q, Kuo Y-H, Sun J, Lee W-C, Lim E, Guo Y-R, Barker DM (2005) Assimilation of Doppler radar observations with a regional 3DVAR system: impact of Doppler velocities on forecasts of a heavy rainfall case. J Appl Meteorol 44:768–788

Xiao Q, Kuo Y-H, Sun J, Lee W-C, Barker DM, Lim E (2007) An approach of radar reflectivity data assimilation and its assessment with the inland QPF of Typhoon Rusa (2002) at landfall. J Appl Meteorol Clim 46:14–22